Precise mass and radius determination for two new and one known Neptune-sized planets around G dwarf hosts

Monthly Notices of the Royal Astronomical Society
MNRAS 549, 1–27 (2026) https://doi.org/10.1093/mnras/staf1958
Advance Access publication 2025 November 08

Precise mass and radius determination for two new and one known Neptune-sized planets around G dwarf hosts

Ilaria Carleo,[1,2★] Grzegorz Nowak,[3] Felipe Murgas,[2,4] Enric Pallé,[2,4] Gaia Lacedelli,[2,4] Thomas Masseron,[2,4] Emily W. Wong,[5] Amadeo Castro-González,[5] Dawid Jankowski,[3] Patrick Eggenberger,[5] James S. Jenkins,[6,7] Krzysztof Goździewski,[3] Vincent Bourrier,[5] Douglas R. Alves,[6,8] José I. Vines,[9] Keivan G. Stassun,[10] Matteo Brogi,[1,11] Sergio Messina,[12] Catherine A. Clark,[13] Karen A. Collins,[14] Hans J. Deeg,[2,4] Elise Furlan,[13] Davide Gandolfi,[11] Samuel Geraldía González,[2,4] Coel Hellier,[15] Artie P. Hatzes,[16] Steve B. Howell,[17] Judith Korth,[5] Emil Knudstrup,[18,19] Jorge Lillo-Box,[20] John H. Livingston,[21,22,23] Jaume Orell-Miquel,[24] Carina Persson,[19] Seth Redfield,[25] Boris Safonov,[26] David Baker,[27] William Cochran,[24] Rafael Delfin Barrena Delgado,[2,4] Allyson Bieryla,[14] Andrew Boyle,[13,28] Pau Bosch-Cabot,[29] Núria Casasayas Barris,[2,4] Stavros Chairetas,[2] David R. Ciardi,[13] Akihiko Fukui,[2,30] Pere Guerra,[29] Kiyoe Kawauchi,[31] Florence Libotte,[2,32,33] Michael B. Lund,[13] Rafael Luque,[34] Eduardo Lorenzo Martín Guerrero de Escalante,[2] Bob Massey,[35] Edward J. Michaels,[36] Giuseppe Morello,[34,37] Norio Narita,[2,21,30] Hannu Parvianien,[2,4] Richard P. Schwarz,[14] Avi Shporer,[38] Monika Stangret[2,4] and Cristilyn N. Watkins[39]

Affiliations are listed at the end of the paper

Accepted 2025 November 6. Received 2025 November 6; in original form 2025 September 11

ABSTRACT

As part of the KESPRINT collaboration, we present the discovery and characterization of three exoplanets in the sub-Neptune to super-Neptune regime, spanning key regions of the exo-Neptunian landscape. TOI-1472 c and TOI-1648 b are newly discovered sub-Neptunes, while TOI-1472 b is a previously known super-Neptune for which we provide an improved mass measurement. These planets have orbital periods of 6–15 d and radii of 2.5–4.1 $R_{\oplus}$, probing regions where planet formation and atmospheric evolution remain poorly understood. We combine *Transiting Exoplanet Survey Satellite* transit photometry with ground-based radial velocities to determine precise masses, radii, and orbital properties. TOI-1472 b has a mass of $18.0^{+0.84}_{-0.85}$ $M_{\oplus}$ and a radius of 4.06 ± 0.10 $R_{\oplus}$, TOI-1472 c has a mass of $21.1^{+0.96}_{-0.99}$ $M_{\oplus}$ and a radius of 3.33 ± 0.08 $R_{\oplus}$, and TOI-1648 b has a mass of $7.4^{+1.1}_{-1.3}$ $M_{\oplus}$ and a radius of $2.54^{+0.14}_{-0.12}$ $R_{\oplus}$. The planets exhibit a range of eccentricities (0.041–0.178), indicating diverse evolutionary histories. TOI-1648 b, with a high transmission spectroscopy metric (TSM $\sim$ 59), is a promising target for atmospheric characterization. Together, these three planets provide precise constraints on the structure, composition, and dynamical evolution of small to intermediate-sized exoplanets, enriching our understanding of the exo-Neptunian landscape.

Key words: techniques: radial velocities – techniques: photometric – exoplanets – planets and satellites: detection.

1 INTRODUCTION

Small exoplanets ($R_P < 4$ $R_{\oplus}$) present many interesting population properties, which still remain widely unexplained to the best of our knowledge. The *Kepler* mission confirmed the earlier finding reported by M. Mayor et al. (2011), who first hinted at the high occurrence rate of sub-Neptunes in close-in orbits (within $\sim$1 au), and revealed a bimodal radius distribution with a gap around 1.7 $R_{\oplus}$, known as the 'radius valley' (T. A. Berger et al. 2018; B. J. Fulton & E. A. Petigura 2018). One of the interpretations is attributed to atmospheric evolution (F. Dai et al. 2019; J. L. Bean, S. N. Raymond & J. E. Owen 2021); planets below the gap (super-Earths) were fully stripped of their primordial hydrogen-dominated atmospheres,[1] while planets above the gap are sub-Neptunes, which

[1]Although we note that recent detections revealed the existence of a handful of low-density super-Earths inconsistent with rocky compositions, likely requiring the presence of a significant amount of volatiles in their atmospheres or interiors (e.g. G. Lacedelli et al. 2021; R. Luque et al. 2022; A. Castro-González et al. 2023; E. Palle et al. 2023).

★ E-mail: ilaria.carleo@inaf.it

Table 1. Stellar properties of TOI-1472 and TOI-1648.

Parameter	TOI-1472	TOI-1648	Ref.
α (ICRS, 2016.0)	00:56:27.42	03:01:36.28	*Gaia* DR3
δ (ICRS, 2016.0)	+48:38:15.06	+69:13:47.72	*Gaia* DR3
μ_α (mas yr^{-1})	103.399	16.187	*Gaia* DR3
μ_δ (mas yr^{-1})	−13.622	5.429	*Gaia* DR3
RV (km s^{-1})	-15.047 ± 0.309	-32.177 ± 0.144	*Gaia* DR3
π (mas)	8.1964	14.3348	*Gaia* DR3
Distance (pc)	121.3097	69.6704	*Gaia* DR3
V (mag)	11.302 ± 0.014	10.43 ± 0.006	TIC v1.8
B (mag)	12.206 ± 0.174	11.448 ± 0.068	TIC v1.8
G (mag)	11.114 ± 0.001	10.1848 ± 0.0003	*Gaia* DR3
$G_{\rm BP} - G_{\rm RP}$ (mag)	1.073	1.173	*Gaia* DR3
TESS (mag)	10.551 ± 0.006	9.583 ± 0.006	TIC v1.8
$J_{\rm 2MASS}$ (mag)	9.794 ± 0.021	8.804 ± 0.032	TIC v1.8
$H_{\rm 2MASS}$ (mag)	9.384 ± 0.023	8.296 ± 0.044	TIC v1.8
$K_{\rm 2MASS}$ (mag)	9.277 ± 0.021	8.183 ± 0.018	TIC v1.8
$S_{\rm MW}$	0.30 ± 0.01	0.25 ± 0.01	This work
$\log R'_{\rm HK}$	-4.79 ± 0.02	-4.95 ± 0.01	This work

Table 2. Summary of *TESS* observations for the two targets.

Target	Sector	CCD number	Camera	Cadence (min)
TOI-1472	17	4	2	2
	57	4	2	2
	58	3	2	2
	84	4	2	2
	84	3	2	2
TOI-1648	18	2	1	2
	19	2	2	2
	25	4	4	2
	52	4	3	2
	59	2	2	2
	79	3	4	2
	86	2	2	2

can be divided into gas-rich super-Earths and water worlds. Gas-rich super-Earths (i.e. Earth-like rocky-iron cores) are thought to form in the inner regions of the protoplanetary disc, which retained their primordial atmospheres without being substantially enriched in volatiles (M. Ikoma & Y. Hori 2012; E. J. Lee & E. Chiang 2016). Water worlds should form beyond the snowline by the accretion of water and rocks – i.e. they should be a scaled-up version of icy moons in the Solar system – followed by inward migration (L. Zeng et al. 2019; J. Venturini et al. 2020). R. Luque & E. Pallé (2022), using a refined sample of small planets orbiting M dwarf hosts, proposed that the radius valley is determined more by the interior composition of exoplanets than by the loss of atmospheric mass. A recent investigation employing atmospheric mass-loss models (J. G. Rogers, H. E. Schlichting & J. E. Owen 2023) has successfully replicated the results reported by R. Luque & E. Pallé (2022) by incorporating spontaneous mass loss (called 'boil-off') following disc dispersal (M. Ikoma & Y. Hori 2012; J. E. Owen & Y. Wu 2016). Overall, sub-Neptunes are situated at the intersection of a modelling degeneracy in interior structure, comprising rock, ices, and/or gas, and they frequently present numerous combinations of these materials capable of aligning with the mass and radius data of individual planets.

At larger radii ($4 < R_{\rm P} < 10\,{\rm R}_\oplus$), other intriguing aspects appear, such as a dearth of Neptune-sized and super-Neptune-sized planets in the closest orbits: the so-called Neptunian desert (e.g. P. Benítez-Llambay, F. Masset & C. Beaugé 2011; G. M. Szabó & L. L. Kiss 2011; T. Mazeh, T. Holczer & S. Faigler 2016). Beyond the desert lies the savanna, where such planets are more commonly found (V. Bourrier et al. 2023). Between these two regions sits the Neptunian ridge, a transitional zone marked by a notable concentration of Neptune-sized planets with orbital periods between ∼3.2 and ∼5.7 d (A. Castro-González et al. 2024a). This accumulation aligns closely with the well-known hot Jupiter pile-up (S. Udry, M. Mayor & N. C. Santos 2003), hinting at possible links in the dynamical histories of intermediate-sized and gas giant planets. Notably, planets located within the desert and ridge tend to exhibit higher densities than those in the surrounding savanna (A. Castro-González et al. 2024b). This density contrast could reflect differences in formation or migration pathways, or enhanced atmospheric loss processes operating in the desert and ridge environments.

In this paper, we report the discovery of two new sub-Neptunes, TOI-1472 c and TOI-1648 b, and present an improved mass measurement for the previously published super-Neptune TOI-1472 b (A. S. Polanski et al. 2024). These systems are of particular interest because they occupy key regions of the small planet and Neptune-sized planet populations, including the radius valley and the Neptunian desert, where formation and evolution processes remain poorly understood. Precise mass and radius determinations for these planets provide important constraints on their interior compositions and atmospheric properties, allowing us to test models of planetary structure, atmospheric loss, and dynamical evolution.

In the following sections, we present the *Transiting Exoplanet Survey Satellite* (*TESS*; G. R. Ricker et al. 2015) photometry, ground-based follow-up observations, spectroscopy, and high-resolution imaging (Section 2), stellar modelling (Section 3), frequency analysis (Section 4), transit and radial velocity (RV) joint fits with planetary system modelling (Section 5), and detailed system characterization (Section 6), followed by our conclusions in Section 7.

2 OBSERVATIONS

2.1 Photometric data

2.1.1 *TESS photometry*

TOI-1472 (TIC 306955329, stellar properties in Table 1) was observed by *TESS* between 2019 October and 2024 November. TOI-1648 (TIC 376353509, Table 1) has been observed between 2019 November and 2024 June. Observations of the targets were conducted with a 2-min cadence. Table 2 summarizes the corresponding *TESS* sectors, CCDs, and camera configurations.

The two candidates, TOI-1472.01 and TOI-1648.01, were identified through the Science Processing Operations Center (SPOC) transit search, which employed an adaptive, noise-compensating matched filter technique (J. M. Jenkins 2002; J. M. Jenkins et al. 2010, 2020). This process flagged a threshold crossing event for each target. Subsequently, a preliminary transit model incorporating limb darkening was fitted to the detected signals (J. Li et al. 2019), followed by a comprehensive battery of diagnostic tests to assess the planetary nature of the transits (J. D. Twicken et al. 2018). Independently, the Quick Look Pipeline (QLP) at the Massachusetts Institute of Technology (MIT) also detected the transit signatures in the full-frame image data (C. X. Huang et al. 2020a, b). These vetting results were carefully reviewed by the *TESS* Science Office, and the signals were confirmed across multiple observing sectors, consistently passing all data validation diagnostics.

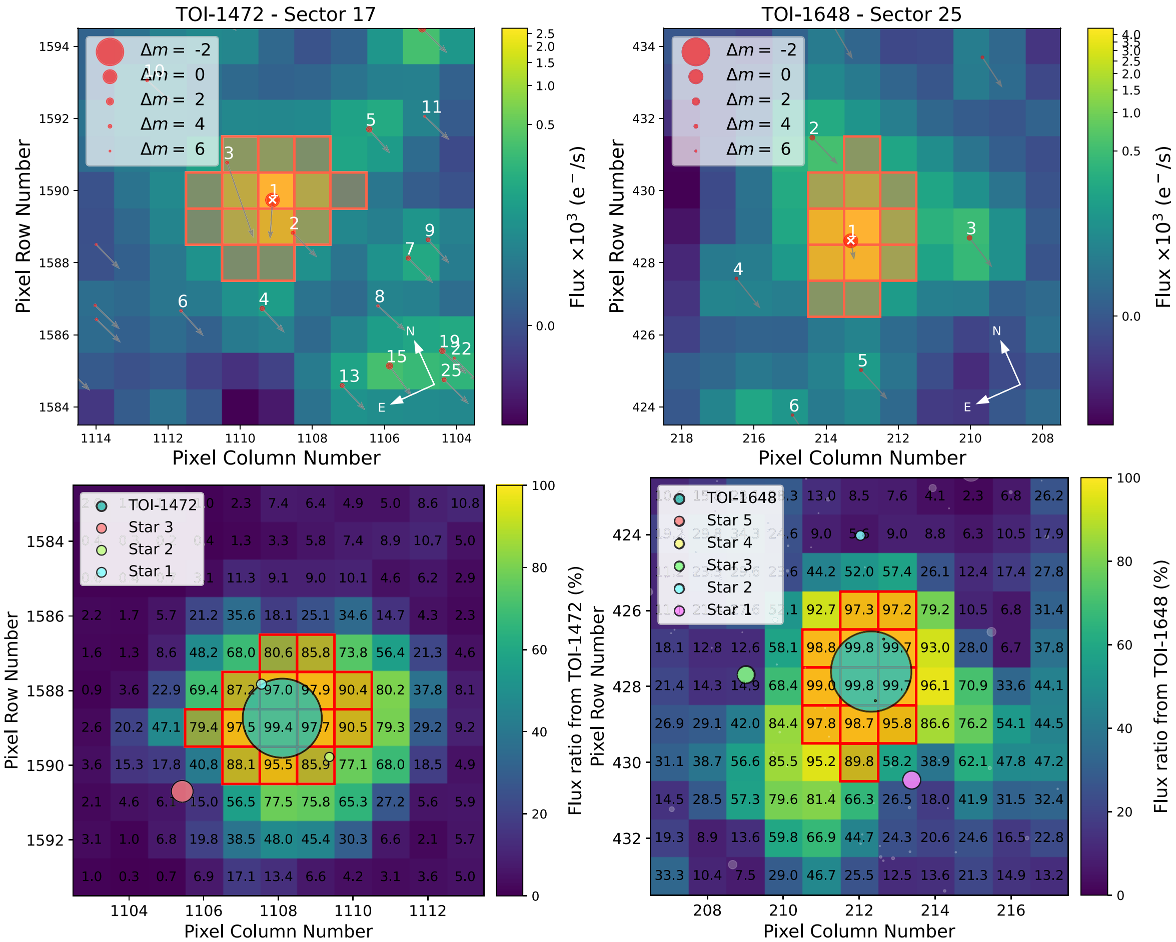

Figure 1. Upper: *TESS* TPFs of Sector 17 for TOI-1472 and Sector 25 for TOI-1648. The colour scale represents electron counts per pixel. Orange squares mark the pixels selected by the *TESS* pipeline for aperture photometry. *Gaia* DR3 sources are overlaid as circles with sizes corresponding to their *G*-band magnitude difference relative to the target, as indicated in the legend. This visualization was created using the TPFPLOTTER code (A. Aller et al. 2020). Grey arrows show the proper motion vectors of all sources in the field. Bottom: *TESS* heat maps for the two targets, produced with TESS-CONT (A. Castro-González et al. 2024b), illustrating the percentage of the target star's flux contained within each pixel.

The additional planet in the TOI-1472 system, discovered later through our RV campaign, was not identified by the transit pipelines during this stage and thus was not designated as a candidate.

TESS photometric data for these targets were processed by both the MIT QLP and the SPOC pipeline (J. M. Jenkins et al. 2016), each applying simple aperture photometry (SAP; J. D. Twicken et al. 2010) to generate light curves. Instrumental systematics were further mitigated using the Pre-search Data Conditioning Simple Aperture Photometry (PDCSAP) algorithm (J. C. Smith et al. 2012; M. C. Stumpe et al. 2012). For our analysis, we retrieved the SPOC PDCSAP light curves from the *Mikulski Archive for Space Telescopes*[2] and used these corrected data in our transit modelling (see Section 5).

We investigated potential flux contamination from nearby sources in the *TESS* data for our targets by first overlaying *Gaia* Data Release 3 (DR3; Gaia Collaboration 2023) catalogue stars onto the target pixel files (TPFs) using the TPFPLOTTER tool (A. Aller et al. 2020) (see Fig. 1). Subsequently, we employed TESS-CONT (A. Castro-González et al. 2024b) to quantify the contribution of these neighbouring sources to the total flux within the SPOC photometric apertures.

[2]https://mast.stsci.edu/

For TOI-1472, the three most contaminant sources are TIC 306955328, TIC 306950348, and TIC 306950347 (Star 2, Star 3, and Star 5 in Fig. 1, respectively), with total flux contributions of 1.34, 0.97, and 0.57 per cent, respectively. For TOI-1648, the three most contaminant sources are TIC 376353519 (Star 2), TIC 376353488 (Star 5), and TIC 376353502 (Star 3), with contributions of 0.45, 0.12, and 0.10 per cent, respectively. Following J. H. Livingston et al. (2018b, a), J. P. Leon et al. (2021), and A. Castro-González et al. (2022), and considering the transit depths of the planetary candidates estimated by the SPOC pipeline, we find that potential deep eclipses of 17–86 per cent (i.e. <100 per cent) in the nearby sources of TOI-1472 and TOI-1648 could generate the observed transit signals. We note that we discard this possibility through follow-up transit (Section 2.1.2) and spectroscopic (Section 2.2) observations and that the PDCSAP data already account for flux dilution, so no additional corrections were necessary.

2.1.2 *TFOP follow-up light curves*

To accurately identify the true sources of the *TESS* signals, correct for any blending effects on transit depths, assess possible wavelength-dependent variations in transit depth, and refine the transit timing,

Table 3. Summary of TFOP ground-based light-curve follow-up.

Telescope	Date (UTC)	Filter	Phot. aper. radius (arcsec)	Nearest *Gaia* DR3 neighbour (arcsec)	Transit coverage
TOI-1472 b					
Adams 0.6 m	2019-12-18	I_c	8.7	17.0	Full
WCO 0.35 m	2020-10-12	Sloan g'	5.3	17.0	Full
LCO MuSCAT3 2.0 m	2021-01-09	g, r, i, z	6.8	17.0	Full
TOI-1648 b					
LCO-McD 1.0 m	2020-08-13	Pan-STARRS z_s	5.4	15.7	Full
LCO-McD 1.0 m	2020-09-04	Sloan i'	10.9	15.7	Full
LCO-McD 1.0 m	2020-09-04	Sloan i'	10.5	15.7	Full

we conducted ground-based photometric follow-up of the fields surrounding TOI-1472 and TOI-1648. This was carried out through the *TESS* Follow-up Observing Program (TFOP; K. Collins 2019).[3] Transit observations were scheduled using the TESS TRANSIT FINDER, a tailored version of the TAPIR software package (E. Jensen 2013).

We observed three transit windows of TOI-1472.01 using the Austin College 0.6-m telescope at Adams Observatory in Sherman, TX, USA (Adams), the 0.35-m telescope at Waffelow Creek Observatory (WCO) in Nacogdoches, TX, USA, and the Las Cumbres Observatory Global Telescope (LCOGT; T. M. Brown et al. 2013) 2-m Faulkes Telescope North at Haleakala Observatory on Maui, Hawai'i. The 2-m LCOGT telescope is equipped with the MuSCAT3 multiband imager (N. Narita et al. 2020). We observed three transit windows of TOI-1648.01 from the LCOGT 1-m network node at McDonald Observatory near Fort Davis, TX, USA (LCO-McD).

Images obtained with LCOGT telescopes were processed using the standard LCOGT BANZAI pipeline (C. McCully et al. 2018), while differential photometry was performed with ASTROIMAGEJ (K. A. Collins et al. 2017). This software was also utilized to calibrate and extract differential photometry from data collected by other participating observatories. For all follow-up light curves, photometric apertures were carefully chosen as small circular regions that excluded flux from the nearest known *Gaia* DR3 neighbours of the target stars. The resulting light-curve data are publicly accessible on the EXOFOP-TESS platform,[4] summarized in Table 3, and jointly modelled as detailed in Section 5.

2.1.3 Ground-based archival data

We examined publicly accessible archival data (already processed light curves) from the All-Sky Automated Survey for Supernovae (ASAS-SN; B. J. Shappee et al. 2014; C. S. Kochanek et al. 2017; K. Hart et al. 2023), the Wide Angle Search for Planets (WASP) transit survey (D. L. Pollacco et al. 2006), and the Zwicky Transient Facility (ZTF; E. C. Bellm et al. 2019; F. J. Masci et al. 2019) to search for rotational variability in the host stars.

For TOI-1472, ASAS-SN has 490 observations spanning ~2030 d in g band, and 200 observations spanning ~1440 d in V band. No significant peak in the generalized Lomb–Scargle (GLS) periodogram (M. Zechmeister & M. Kürster 2009) for the time series was found in the ASAS-SN data sets. The WASP photometry has one season of coverage of TOI-1472, spanning 130 d in 2007, amounting to 4000 photometric data points. Analysing the light curve using methods from P. F. L. Maxted et al. (2011), we find no rotational modulation, with a 95 per cent confidence upper limit of 2 mmag. For this star, there were no ZTF data.

TOI-1648 has ASAS-SN data, no WASP coverage, and no ZTF time series. The ASAS-SN observations consist of 480 g-band data points spanning ~1990 d, while the V-band observations have 180 observations spanning ~2500 d. As was the case for TOI-1648, we did not find any significant peak in the periodogram of the time series that could belong to the rotation period of the star.

2.2 Spectroscopic data

The two stars were observed as part of the KESPRINT collaboration,[5] which aims to measure the masses of small and intermediate-sized planets. Observations were conducted using the High Accuracy Radial velocity Planet Searcher for the Northern hemisphere (HARPS-N) visible spectrograph (R. Cosentino et al. 2014) at the Telescopio Nazionale Galileo (TNG) in La Palma, Spain, under the programs CAT19A_162, CAT21A_119, and CAT22A_111 (PI: Nowak), ITP19_1 (PI: Palle), CAT20B_80 (PI: Casasayas), CAT23A_52 and CAT23B_74 (PI: Carleo).

TOI-1472. We collected 52 HARPS-N RVs for TOI-1472 between 2020 January 13 UT and 2020 February 13 UT, with an exposure time of 1800 s, and an average signal-to-noise ratio (SNR) per pixel of 48. We used the offline version of HARPS-N Data Reduction Software (DRS) through the YABI web application (A. A. Hunter et al. 2012) installed at IA2 Data Center[6] in order to extract the RVs and activity indicators. For TOI-1472, we used a K5 mask template, as it better matches the star's spectral type, and a cross-correlation function (CCF) width of 30 km s^{-1}. We obtained an average precision of 1.7 m s^{-1}. The list of RVs is presented in Table A1, together with the chromospheric activity indexes, S-index, and log $R'_{\rm HK}$.

For the analysis, we also incorporated 22 HIRES RV measurements (with a typical RV uncertainty of 1.7 m s^{-1}) from A. S. Polanski et al. (2024), who reported the discovery of planet TOI-1472 b.

TOI-1648. We collected 53 HARPS-N RVs between 2020 October 10 UT and 2023 March 10 UT with an exposure time of 1800 s and an average SNR of 67. As for TOI-1472, we used a K5 mask and 30 km s^{-1} of CCF width to extract the RVs with YABI. We obtained an average RV uncertainty of 1.2 m s^{-1}. Table A4 lists the RVs and activity indexes for TOI-1648.

Activity-related parameters such as log $R'_{\rm HK}$, the S-index, bisector span, CCF contrast, and CCF full width at half-maximum (FWHM) were extracted from the HARPS-N DRS (Table A2 for TOI-1472, Table A5 for TOI-1648). For log $R'_{\rm HK}$, we adopted the $B-V$

[3] https://tess.mit.edu/followup
[4] https://exofop.ipac.caltech.edu/tess/
[5] www.kesprint.science
[6] https://www.ia2.inaf.it

colour calculated from the magnitude values in Table 1. Additional diagnostics – including the chromatic index (CRX), differential line width (dLW), H α index, and sodium doublet lines (Na I and Na II) – were derived using the SERVAL pipeline (M. Zechmeister et al. 2018, Table A3 for TOI-1472, Table A6 for TOI-1648).

2.3 High-resolution imaging

To evaluate potential contamination from bound or unbound stellar companions that could bias the derived planetary radii (J. Lillo-Box, D. Barrado & H. Bouy 2012, 2014; D. R. Ciardi et al. 2015; E. Furlan & S. B. Howell 2017, 2020; J. Lillo-Box et al. 2024), we followed standard validation procedures by obtaining high-resolution imaging of the TOIs (*TESS* Objects of Interest) using optical speckle, lucky imaging, and/or near-infrared adaptive optics (AO) techniques.

2.3.1 Optical speckle imaging

TOI-1472 and TOI-1648 were observed on 2021 September 9 UT and 2020 October 29 UT, respectively, using the speckle polarimeter mounted on the 2.5-m telescope at the Caucasian Observatory of the Sternberg Astronomical Institute, Lomonosov, Moscow State University. Observations were performed with an Andor iXon 897 Electron Multiplying CCD detector (B. S. Safonov, P. A. Lysenko & A. V. Dodin 2017). For TOI-1472, imaging was conducted in the I_c band, yielding an angular resolution of 0.083 arcsec. For TOI-1648, a filter with a bandpass of 50 nm centred on 625 nm was used with an angular resolution of 0.063 arcsec. No nearby stellar companions were detected in either case. At separations of 0.25 and 1.0 arcsec, the achieved contrast limits were $\Delta I_c = 4.1$ and 5.3 mag for TOI-1472, and $\Delta I_c = 4.6$ and 6.0 mag for TOI-1648.

Both TOI-1472 and TOI-1648 were also observed on 2020 December 3 UT and 2021 October 22 UT, respectively, using the `Alopeke high-resolution speckle instrument on the Gemini North 8-m telescope (N. J. Scott et al. 2021). `Alopeke provides simultaneous speckle imaging in two bands (562 and 832 nm) with output data products including a reconstructed image with robust contrast limits on companion detections. Five sets of 1000 X 0.06-s images were obtained and processed along with the point spread function standards HR 0189 (TOI-1472) and HR 0829 (TOI-1648) in our standard reduction pipeline (see S. B. Howell et al. 2011) for each star. Fig. 2 shows the final 5σ magnitbl4tude contrast curves and the 832 nm reconstructed speckle image. We find that TOI-1472 and TOI-1648 are single stars with no companion brighter than 5–8 mag below that of the target star from the 8-m telescope diffraction limit (20 mas) out to 1.2 arcsec. At the distances of TOI-1472 ($d = 122$ pc) and TOI-1648 ($d = 70$ pc), these angular limits correspond to spatial limits of 2.4–146 au and 1.4–84 au, respectively.

2.3.2 Lucky imaging

We observed TOI-1648 using the AstraLux lucky-imaging camera (F. Hormuth et al. 2008) installed at the 2.2-m telescope in Calar Alto (Almería, Spain). Observations were performed on the night of 2020 February 26 under the AstraLux follow-up of the *TESS* planet candidates program (PI: J. Lillo-Box). The observations and data analysis corresponding to this target are detailed in J. Lillo-Box et al. (2024). In summary, we found no stellar companions around this target with a 95 per cent sensitivity limit at 0.5 arcsec of 4.3 mag fainter than the target. This implies a probability of an undetected source capable of mimicking the transit signal is 0.29 per cent (J. Lillo-Box, D. Barrado & H. Bouy 2014).

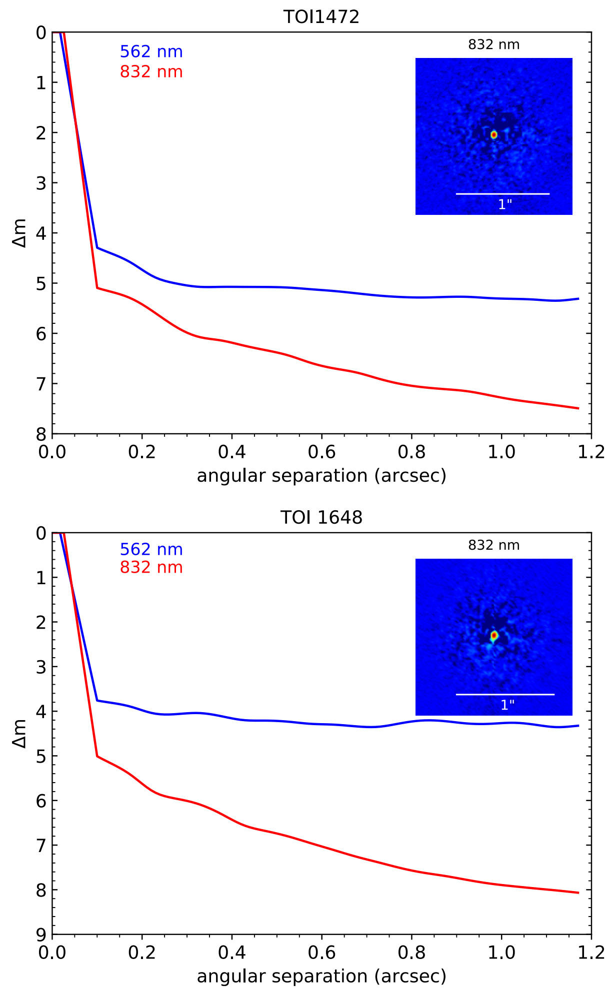

Figure 2. Reconstructed `Alopeke speckle images and 5σ contrast limits from simultaneous diffraction-limited exposure sequences using the 562 nm filter on the blue camera and the 832 nm filter on the red camera. No nearby sources are detected.

2.3.3 Near-infrared AO imaging

Observations of TOI-1472 and TOI-1648 were made on 2020 May 28 UT and 2020 September 9 UT with the NIRC2 instrument on Keck-II (10 m) behind the natural guide star AO system (P. Wizinowich et al. 2000). TOI-1472 was also observed with the ShARCS camera on the Shane 3 m at Lick Observatory (Dressing et al., in preparation). The pixel scales of the ShARCS and NIRC2 instruments are 0.033 and 0.009942 arcsec pixel^{-1}, respectively. Observations at Lick Observatory were taken using a standard five-point quincunx dither pattern, while the Keck observations employed a three-point dither pattern designed to avoid the lower left quadrant of the detector. The reduced science frames were subsequently combined into final mosaiced images, achieving angular resolutions of approximately 0.3 arcsec for ShARCS and 0.05 arcsec for NIRC2.

To assess the sensitivity of the final combined AO images, we injected artificial sources at regular azimuthal intervals of 20° around the primary target, placing them at radial distances corresponding to integer multiples of the target's FWHM (E. Furlan et al. 2017). The flux of each simulated source was adjusted until it was detected with a 5σ significance level using standard aperture photometry. At each separation, the 5σ contrast limit was calculated as the average

Table 4. Spectroscopic parameters for TOI-1472 and TOI-1648, as derived in this work.

Method	$T_{\rm eff}$ (K)	$\log g_\star$ (cgs)	[Fe/H] (dex)	$\xi_{\rm t}$ (km s^{-1})	Mass (M$_\odot$)	Radius (R$_\odot$)	Age (Gyr)
			TOI-1472				
BACCHUS + PARAM[a]	5100 ± 50	4.5 ± 0.1	0.27 ± 0.09	0.9 ± 0.1	0.87 ± 0.06	0.84 ± 0.02	...
SPECIES + ARIADNE	5106 ± 50	4.2 ± 0.1	0.19 ± 0.04	0.3 ± 0.2	0.89 ± 0.03	0.84 ± 0.01	$3.1^{+4.3}_{-2.2}$
SED	...	...	...	...	0.90 ± 0.05	0.83 ± 0.02	3.1 ± 0.4
			TOI-1648				
BACCHUS + PARAM[a]	4850 ± 50	4.5 ± 0.1	0.20 ± 0.09	0.8 ± 0.1	0.83 ± 0.06	0.81 ± 0.02	...
SPECIES + ARIADNE	5125^{+126}_{-40}	4.7 ± 0.2	0.12 ± 0.04	1.2 ± 0.1	$0.88^{+0.02}_{-0.07}$	0.79 ± 0.01	$0.5^{+7.7}_{-0.5}$ [b]
SED	...	...	...	...	0.82 ± 0.05	0.83 ± 0.02	5.7 ± 0.4

[a]Adopted values for the joint fit in Section 5. [b]The young limit of this age can be ruled out by the lack of stellar rotation signal in the *TESS* data (see Section 4).

detection threshold of all injected sources, while the associated uncertainty was derived from the root mean square variation of the detection limits across the azimuthal positions.

3 STELLAR MODELLING

3.1 Method 1: BACCHUS + PARAM

We performed a consistent spectroscopic analysis of the stellar parameters using the updated version of the BACCHUS code (T. Masseron, T. Merle & K. Hawkins 2016; C. R. Hayes et al. 2022), which is based on MARCS model atmospheres (B. Gustafsson et al. 2008). The analysis was carried out using coadded HARPS-N spectra. Stellar effective temperatures ($T_{\rm eff}$) were determined by minimizing any correlation between the abundances of Fe I lines and their excitation potentials. Surface gravities ($\log g$) were inferred by enforcing ionization equilibrium between Fe I and Fe II lines. Microturbulent velocities ($\xi_{\rm t}$) were obtained by ensuring that there was no trend between iron abundances and the equivalent widths of the lines. The metallicity ([Fe/H]) was computed as the mean abundance from Fe I lines.

To estimate projected stellar rotational velocities ($v \sin i$), we measured the average broadening of iron lines in the HARPS-N spectra, after accounting for instrumental and thermal broadening. Macroturbulent velocity was neglected due to the cool temperatures of the stars. For all targets, this analysis yielded only upper limits on $v \sin i$ (<3.5 km s^{-1}), consistent with slow rotation periods ($\gtrsim 13$ d).

Stellar masses and radii were subsequently derived using the PARAM Bayesian framework (A. Bressan et al. 2012; T. S. Rodrigues et al. 2017), incorporating spectroscopic temperatures and luminosities derived from updated *Gaia* parallaxes. Since PARAM does not account for systematic differences between various stellar evolution models, we employed both MESA and PARSEC isochrones to estimate the impact of model-dependent uncertainties. We added the discrepancy between the two sets of outputs to the formal PARAM errors to provide a more realistic uncertainty estimate. While this approach reduces model-related systematics, it may still underestimate the total error budget for stellar radius and luminosity, as discussed by J. Tayar et al. (2022). The final stellar parameters are summarized in Table 4.

3.2 Method 2: SPECIES + ARIADNE

We independently derived stellar atmospheric and bulk parameters using a two-step approach that combines the SPECIES code (M. G. Soto & J. S. Jenkins 2018) with the ARIADNE framework (J. I. Vines & J. S. Jenkins 2022). SPECIES was applied to the coadded high-resolution spectra to extract fundamental spectroscopic parameters, which were then used as priors in ARIADNE – a Bayesian Model Averaging (BMA) tool designed to infer stellar properties of nearby stars.

SPECIES derives $T_{\rm eff}$, $\log g$, [Fe/H], and $\xi_{\rm t}$ by first measuring the equivalent widths of selected Fe I and Fe II absorption lines. These measurements are used in conjunction with interpolated ATLAS9 stellar atmosphere models (F. Castelli & R. L. Kurucz 2004) and the radiative transfer code MOOG (C. Sneden 1973) to iteratively solve for atmospheric properties. The method enforces excitation and ionization equilibrium by minimizing any dependence of iron abundances on excitation potential and reduced equivalent width (W/λ), assuming local thermodynamic equilibrium.

In parallel, $v \sin i$ is estimated by comparing observed absorption features with synthetic line profiles, adjusted using empirical calibrations based on stellar temperature. These spectroscopic outputs are then fed into ARIADNE, which incorporates multiple stellar evolution models under a BMA framework to yield posterior distributions for global stellar parameters such as radius and mass, while marginalizing over model-dependent uncertainties.

The obtained values are listed in Table 4.

3.3 Method 3: spectral energy distribution

We performed a broad-band spectral energy distribution (SED) analysis for each star, incorporating the precise parallaxes from *Gaia* DR3 to derive empirical estimates of stellar radii (K. G. Stassun & G. Torres 2016; K. G. Stassun, K. A. Collins & B. S. Gaudi 2017; K. G. Stassun et al. 2018). Photometric data were compiled from several sources: near-infrared $JHK_{\rm S}$ bands from Two Micron All-Sky Survey, mid-infrared $W1$–$W4$ from *Wide-field Infrared Survey Explorer*, optical $G_{\rm BP}$ and $G_{\rm RP}$ magnitudes from *Gaia*, and ultraviolet fluxes from *Galaxy Evolution Explorer* where available. The absolute flux-calibrated *Gaia* spectra were included in the analysis. This photometric coverage extends across a wide wavelength baseline, typically from 0.4 to 10 µm and, in some cases, reaching from 0.2 to 20 µm (see Fig. 3).

The observed SEDs were modelled using synthetic spectra from the PHOENIX atmosphere grid (T. O. Husser et al. 2013), adopting the stellar effective temperature, metallicity, and surface gravity from our spectroscopic analysis. Interstellar extinction (A_V) was treated as a free parameter in the fit, but constrained not to exceed the line-of-sight reddening predicted by the Galactic dust maps of D. J. Schlegel, D. P. Finkbeiner & M. Davis (1998).

By integrating the best fit, dereddened model SED, we computed the bolometric flux ($F_{\rm bol}$) received at Earth. Combining this flux with the *Gaia* parallax yields the bolometric luminosity ($L_{\rm bol}$), and the

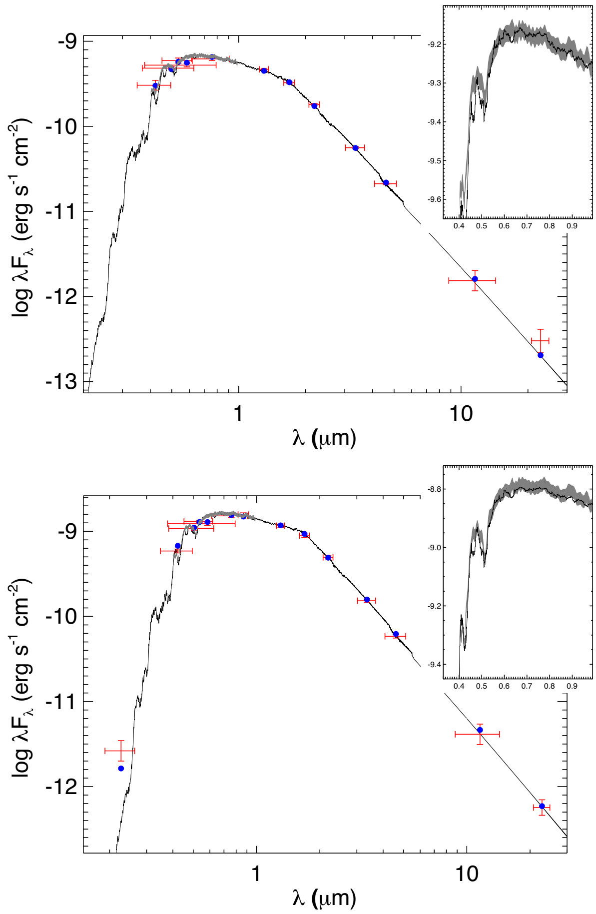

Figure 3. SEDs of TOI-1472 (top) and TOI-1648 (bottom). The red markers indicate the observed photometric data, with horizontal bars denoting the effective bandwidth of each filter. Blue points represent the synthetic fluxes derived from the best-fitting PHOENIX stellar atmosphere model, shown in black. In the inset, the absolute flux-calibrated *Gaia* spectrum is displayed as a grey shaded region.

stellar radius ($R_\star$) was then calculated via the Stefan–Boltzmann law. Stellar masses were inferred using empirical calibrations of G. Torres, J. Andersen & A. Giménez (2010).

Chromospheric activity indicators ($R'_{\rm HK}$) were used to estimate stellar ages using the empirical age–activity relations of E. E. Mamajek & L. A. Hillenbrand (2008). The related age uncertainties are the formal uncertainty in the adopted relation itself and do not include potential systematic errors between different relations, which are typically of the order of 1 Gyr. These same calibrations also provide gyrochronology-based estimates of stellar rotation periods.

Fig. 3 displays the SED fits for each star. A summary of the derived physical parameters is provided in Table 4, with individual values discussed below.

TOI-1472: the best fit has $A_V = 0.03 \pm 0.03$, with a reduced χ^2 of 1.3, $F_{\rm bol} = 9.10 \pm 0.21 \times 10^{-10}$ erg s^{-1} cm^{-2}, $L_{\rm bol} = 0.4225 \pm 0.0099$ L$_\odot$, and estimated rotation period of 37 ± 2 d. TOI-1648: the best fit has $A_V = 0.01 \pm 0.01$, with a reduced χ^2 of 1.4, $F_{\rm bol} = 2.254 \pm 0.019 \times 10^{-9}$ erg s^{-1} cm^{-2}, $L_{\rm bol} = 0.3420 \pm 0.0028$ L$_\odot$, and estimated rotation period of 45 ± 2 d.

We computed the galactic U, V, W local rest system velocities for both TOI-1472 and TOI-1648 using the *Gaia* DR3 astrometry and RV values given in Table 1. We then used these absolute space velocities to compute the galactic dynamic stellar population membership of the star using the formalism originally developed by D. R. H. Johnson & D. R. Soderblom (1987). Both stars are clear dynamical members of the galactic thin disc population. This agrees with their [Fe/H] abundances as given in Table 4.

It is noteworthy that the three methods do not yield consistent results for all parameters. This discrepancy arises primarily from the different prescriptions of microturbulence adopted by each code, which subsequently propagate into the determination of other stellar parameters. The microturbulence parameter is empirical in nature, introduced to account for the effects of unresolved velocity fields on the derived abundances, and can therefore, in principle, be adjusted with some degree of freedom. Nevertheless, the values inferred by BACCHUS are more closely aligned with those typically observed in stars of comparable spectral type, which motivates our preference for adopting the BACCHUS results in the determination of the planetary characteristics. It is worth emphasizing that when the BACCHUS parameters are used as input for the ARIADNE analysis, the resulting stellar mass and radius are in excellent agreement with those obtained using PARAM. Furthermore, irrespective of the adopted set of parameters, the inferred stellar mass and radius remain consistent within the quoted uncertainties.

4 FREQUENCY ANALYSIS

To explore periodic signals within the *TESS* photometry, RV data, and stellar activity indicators, we conducted a frequency analysis using GLS periodograms for the two systems.

We searched for signs of stellar rotation in the *TESS* light curves, but none of the targets exhibited significant periodic modulation. In contrast, the RV data revealed prominent peaks [above the false alarm probability (FAP) = 1 per cent] aligned with the orbital periods of the detected planets (see Fig. 4). The periodograms of the activity indicators showed a range of peaks, with varying significance across different diagnostics.

Given the lack of a consistent rotation period across activity tracers, we adopted a Gaussian process (GP) model in the joint RV-photometry fit (Section 5) with a broad, non-informative prior on the stellar rotation period, spanning from 2 to 100 d. This approach accommodates the uncertainty and diversity of the activity signals. In the periodogram figures, two shaded bands are used to guide interpretation: the red band marks the rotation period estimated from the SED (Section 3.3), while the orange band reflects the posterior distribution of the GP-inferred rotation period.

For TOI-1472, the GP-inferred rotation period is nearly twice the value estimated from the SED. Both values, however, are consistent with prominent peaks observed in the activity periodograms, supporting their physical plausibility. Additionally, for TOI-1472, the periodogram reveals a highly significant peak (above FAP = 1 per cent) at approximately 15 d, which does not correspond to any features in the periodograms of the stellar activity indicators. A visual inspection of the *TESS* data further revealed additional transits, providing evidence for a second planet in the system. Fig. 5 shows the TOI-1472 *TESS* time series in Sectors 17, 57, and 58. *TESS* did not detect planet TOI-1472 c earlier because its transits during Sector 17 coincided with data gaps. In Sectors 57 and 58, although two full transits are visible, one transit is only partial, and another is completely blended with the transit of planet TOI-1472 b, resulting in a deeper combined signal. These factors contributed to the initial non-detection of planet TOI-1472 c by the SPOC pipeline.

In the case of TOI-1648, the GP posterior shows a bimodal distribution with peaks around 32 and 64 d, whereas the SED-based

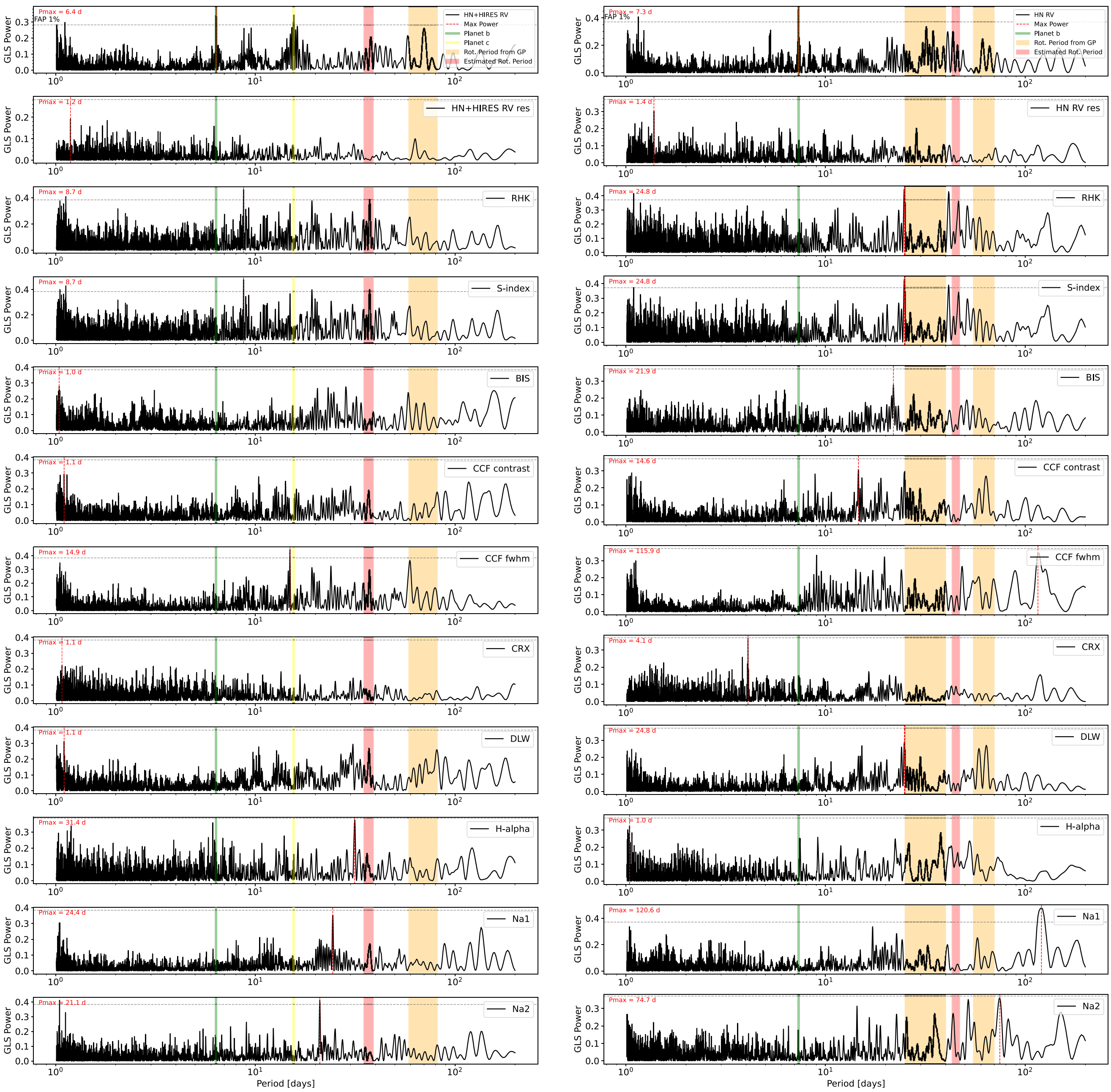

Figure 4. GLS periodograms for TOI-1472 (left) and TOI-1648 (right). Periodograms are shown for the RV data, the residuals after subtracting the fitted planetary signal, and all stellar activity indicators derived from the HARPS-N DRS (log R'_{HK}, S-index, bisector span, CCF contrast, and CCF FWHM) and from the SERVAL pipeline (CRX, dLW, H α, and the Na I and Na II lines). For TOI-1472, where two data sets (HARPS-N and HIRES) are available, the RVs have been shifted to a common median RV prior to computing the GLS periodogram. The orange shaded area denotes the stellar rotation period inferred from the joint GP analysis using wide period priors (2–100 d), as detailed in Section 5. The red shaded area marks the rotation period derived from the SED-based analysis (Section 3.3). The red dashed line indicates the location of the dominant peak in each periodogram, while the green and yellow lines denote the orbital periods of planets TOI-1472 b and TOI-1472 c, respectively. For TOI-1648, the rotational modulation exhibits a double-peaked structure in the GP posterior.

estimate lies between these two values. All these periods are consistent with signals in the activity indicators, suggesting possible harmonics. Motivated by the presence of a significant peak around 120 d in some of the activity indices, the prior range on the stellar rotation period was extended from 2–100 d to 2–200 d. With this broader range, an additional peak in the GP posterior emerges around 160 d (five times the rotation period of 32 d). This long-period signal may correspond to longer time-scale activity modulations or harmonics.

5 PLANET SYSTEM PARAMETERS: JOINT FIT

To derive the planetary system parameters, we conducted a comprehensive joint fit of the RV measurements alongside the photometric transit data. This analysis was performed using the PYORBIT package[7] (L. Malavolta et al. 2016, 2018). For modelling the transit light

[7]https://github.com/LucaMalavolta/PyORBIT

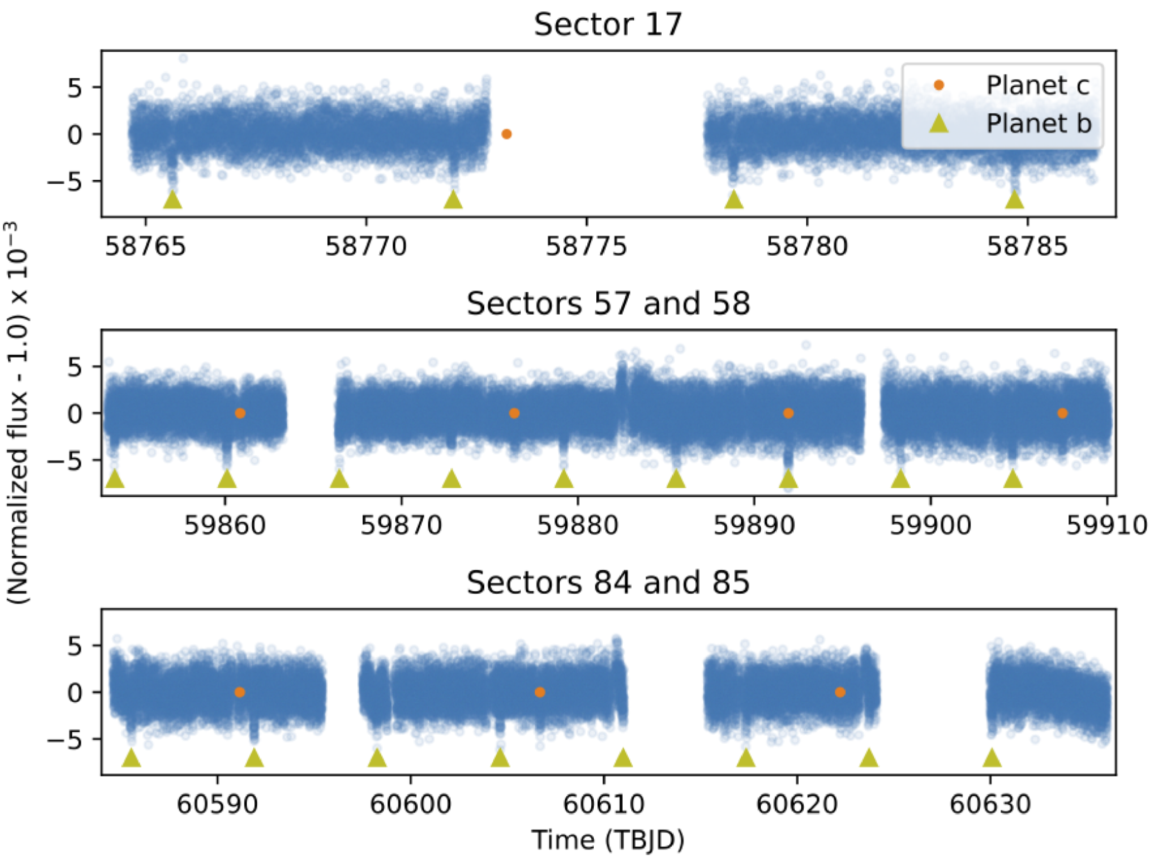

Figure 5. *TESS* time series for TOI-1472 during Sectors 17, 57, 58, 84, and 85. The green triangle indicates the transits of TOI-1472 b, while the orange dots indicate TOI-1472 c's transits.

curves, we employed the BATMAN code (L. Kreidberg 2015), which implements the quadratic limb-darkened transit model from K. Mandel & E. Agol (2002). Each transit included a local polynomial trend to account for residual systematics, as the *TESS* light curves had not been pre-detrended. The fitted transit parameters included the time of inferior conjunction (T_c), orbital period (P), impact parameter (b), orbital eccentricity (e), and argument of periastron (ω), using the J. Eastman, B. S. Gaudi & E. Agol (2013) parametrization of eccentricity as $\sqrt{e}\cos\omega$ and $\sqrt{e}\sin\omega$. Quadratic limb darkening coefficients were parametrized following D. M. Kipping (2013). Additional free parameters comprised the scaled planetary radius ($R_P/R_\star$) and the stellar mass ($M_\star$) and radius ($R_\star$). Gaussian priors on the stellar mass and radius were imposed based on the spectroscopic analysis presented in Section 3.1. Limb darkening priors were derived from PYLDTK[8] (T. O. Husser et al. 2013; H. Parviainen & S. Aigrain 2015), taking into account the bandpasses of the different instruments, and inflating the uncertainties to 0.1 to accommodate possible discrepancies between observed and theoretical limb darkening (J. A. Patel & N. Espinoza 2022). The impact parameter was treated as a free parameter, and no dilution factor was applied since the PDCSAP fluxes were already corrected for crowding effects (see Section 2).

Instrumental offsets, as well as additional sources of noise such as stellar activity and systematics, were accounted for by including individual RV zero-point offsets and jitter terms in the model. Parameter exploration was carried out using the dynamic nested sampling algorithm implemented in DYNESTY[9] (J. S. Speagle 2020; S. Koposov et al. 2022), with 1000 live points to efficiently sample the parameter space. For each system, we compared fits both with and without GP regression. When included, the GP modelling utilized the GEORGE package (S. Ambikasaran et al. 2015), applying a quasi-periodic kernel as described by S. K. Grunblatt, A. W. Howard & R. D. Haywood (2015). In this kernel, the hyperparameters are: h, the amplitude of correlated noise; θ, representing the stellar rotation period; ω, the inverse length-scale related to the evolution of active regions; and λ, the decay time-scale of correlations. Model comparison was based on Bayesian evidence ($\log \mathcal{Z}$) computed through nested sampling. In all cases, the GP-enhanced model was strongly preferred, with a difference in log-evidence ($\Delta \log \mathcal{Z}$) exceeding 3, indicating decisive support for including stellar activity modelling.

For TOI-1472, the planetary system parameters were derived through a two-planet fit, since we identified a second planet from the RV data, combined with a GP. The results are detailed in Table 5, and the RV and transit fits, along with overlaid models, are depicted in Figs 6 and 7. TOI-1472 b has a mass of $18.05^{+0.84}_{-0.85}$ M$_\oplus$, a radius of 4.058 ± 0.098 R$_\oplus$, an orbital period of $\sim$6.36 d, and an eccentricity of 0.041 ± 0.002. We find TOI-1472 c to have a mass of $21.13^{+0.96}_{-0.99}$ M$_\oplus$, a radius of 3.334 ± 0.080 R$_\oplus$, an orbital period of $\sim$15.54 d, and an eccentricity of 0.172 ± 0.002.

For TOI-1648, the system parameters obtained from a one planet plus Gaussian process (1p + GP) fit are listed in Table 6. The planet has a mass of $7.4^{+1.1}_{-1.3}$ M$_\oplus$ and a radius of $2.54^{+0.14}_{-0.12}$ R$_\oplus$. It orbits its host

[8]https://github.com/hpparvi/ldtk

[9]https://github.com/joshspeagle/dynesty

Table 5. TOI-1472 parameters from the transit and RV joint fit, obtained with the model 2p + GP (two planets plus Gaussian process).

Parameter	Prior[a] (Planet b/Planet c)	Value[b] Planet b	Value[b] Planet c
Model parameters			
Orbital period P_{orb} (d)	$\mathcal{U}[5.9, 6.7]$/$\boldsymbol{\mathcal{U}}$**[10.0, 19.0]**	$6.36338574 \pm 1.1 \times 10^{-7}$	$15.5381747 \pm 3.1 \times 10^{-6}$
Transit epoch T_0 (BJD – 245 0000)	$\mathcal{U}[9694.0, 9695.0]$/$\mathcal{U}[9688.9, 9690.9]$	9694.66385 ± 0.00002	$9689.93567^{+0.00012}_{-0.00010}$
$\sqrt{e}\sin\omega_\star$	$\mathcal{U}(-1, 1)$	$0.182^{+0.005}_{-0.004}$	$-0.118^{0.007}_{-0.008}$
$\sqrt{e}\cos\omega_\star$	$\mathcal{U}(-1, 1)$	0.088 ± 0.004	0.397 ± 0.002
Scaled planetary radius $R_{\mathrm{p}}/R_\star$	$\mathcal{U}[0, 0.5]$	0.044 ± 0.001	0.036 ± 0.001
Impact parameter, b	$\mathcal{U}[0, 1]$	$0.014^{+0.029}_{-0.014}$	0.657 ± 0.003
RV semi-amplitude variation K (m s^{-1})	$\mathcal{U}[0, 300]$	$6.841^{+0.017}_{-0.019}$	6.030 ± 0.019
Derived parameters			
Planet radius (R_{J})	...	0.362 ± 0.009	0.298 ± 0.007
Planet radius ($\mathrm{R}_\oplus$)	...	4.058 ± 0.098	3.334 ± 0.080
Planet mass (M_{J})	...	0.057 ± 0.003	0.067 ± 0.003
Planet mass ($\mathrm{M}_\oplus$)	...	$18.05^{+0.84}_{-0.85}$	$21.13^{+0.96}_{-0.99}$
Eccentricity e	...	0.041 ± 0.002	0.172 ± 0.002
Scaled semimajor axis $a/R_\star$	...	$18.565^{+0.027}_{-0.034}$	$33.665^{+0.050}_{-0.062}$
Semimajor axis a (au)	...	0.064 ± 0.002	0.116 ± 0.003
ω_{P} (°)	...	50.5 ± 0.1	164.7 ± 0.2
Orbital inclination i (°)	...	$89.954^{+0.044}_{-0.092}$	$88.906^{+0.004}_{-0.005}$
Transit duration T_{41} (d)	...	0.114 ± 0.001	0.118 ± 0.001
Transit duration T_{32} (d)	...	0.104 ± 0.001	0.104 ± 0.001
Calculated parameters			
Equilibrium temperature[c] T_{eq} (K)		891 ± 20	662 ± 13
Planetary density ρ_{P} (g cm^{-3})		1.49 ± 0.13	3.14 ± 0.27
Other system parameters			
Jitter term $\sigma_{\text{HARPS-N}}$ (m s^{-1})	$\mathcal{U}[0, 60]$	$1.678^{+0.015}_{-0.016}$	
Jitter term σ_{HIRES} (m s^{-1})	$\mathcal{U}[0, 60]$	$1.904^{+0.045}_{-0.050}$	
Limb darkening q_1	$\mathcal{N}[0.451, 0.1]$	0.490 ± 0.002	
Limb darkening q_2	$\mathcal{N}[0.121, 0.1]$	0.124 ± 0.003	
Stellar activity GP model parameters			
$h_{\text{HARPS-N}}$ (m s^{-1})	$\mathcal{U}[0, 100]$	$3.427^{+0.028}_{-0.031}$	
h_{HIRES} (m s^{-1})	$\mathcal{U}[0, 100]$	$3.798^{+0.046}_{-0.040}$	
λ (d)	$\mathcal{U}[5, 2000]$	$205.0^{+3.3}_{-3.8}$	
ω	$\mathcal{U}[0.01, 0.60]$	$0.217^{+0.003}_{-0.002}$	
θ (P_{rot}) (d)	$\mathcal{U}[2, 100]$	69^{+13}_{-10}	
Results from internal structure retrievals			...
Envelope-to-planet mass fraction (per cent)	...	$6.3^{+1.8}_{-1.5}$	...
Core and mantle mass fraction (per cent)	...	$93.7^{+1.5}_{-1.8}$	...
Results from atmospheric evolution			
Maximum initial mass ($\mathrm{M}_\oplus$)	...	$27.7^{+1.2}_{-1.2}$	...
Initial envelope mass ($\mathrm{M}_\oplus$)	...	$10.7^{+0.6}_{-0.7}$	...
Initial envelope-to-planet mass fraction (per cent)	...	$38.6^{+4.1}_{-4.0}$	...
Initial radius ($\mathrm{R}_\oplus$)	...	$10.2^{+0.2}_{-0.2}$	...

[a] $\mathcal{U}[a, b]$ refers to uniform priors between a and b, $\mathcal{N}[a, b]$ to Gaussian priors with median a and standard deviation b.
[b] Parameter estimates and corresponding uncertainties are defined as the median and the 16th and 84th percentiles of the posterior distributions.
[c] $T_{\mathrm{eq}} = T_\star\ (R_\star/2a)^{1/2}\ [f(1 - A_{\mathrm{B}})]^{1/4}$, assuming efficient recirculation $f = 1$ and a null Bond albedo ($A_{\mathrm{B}} = 0$).

star with a period of ∼7.33 d and has an eccentricity of $0.178^{+0.075}_{-0.053}$. The transit and RV fits are shown in Fig. 8.

6 DETAILED CHARACTERIZATION OF THE SYSTEMS

In the previous sections, we presented the discovery of two new *TESS* planets, TOI-1472 c and TOI-1648 b, and an improved mass determination for the previously known planet TOI-1472 b, all orbiting G-type stars. In the following subsections, we detail and discuss the bulk properties and system characterization of each planet.

6.1 TOI-1472 b and TOI-1472 c

We determined the mass of TOI-1472 b to be $18.05^{+0.84}_{-0.85}$ $\mathrm{M}_\oplus$ and the radius to be 4.058 ± 0.098 $\mathrm{R}_\oplus$ (see mass–radius diagram in Fig. 9), which are consistent with the values reported in the discovery paper (A. S. Polanski et al. 2024), although we refined the planetary parameters with significantly enhanced precision. Compared to the previous estimates (16.5 ± 5.1 $\mathrm{M}_\oplus$ and 4.16 ± 0.16 $\mathrm{R}_\oplus$), our mass and radius measurements improve the precision by factors of ∼6 and ∼1.6, respectively; the detection significance increases from 3.2σ to 21.2σ for the mass and from 26.0σ to 41.4σ for the radius; and the relative uncertainties are reduced from 31 to 4.7 per cent for the mass and from 3.85 to 2.41 per cent for the radius. The improvement

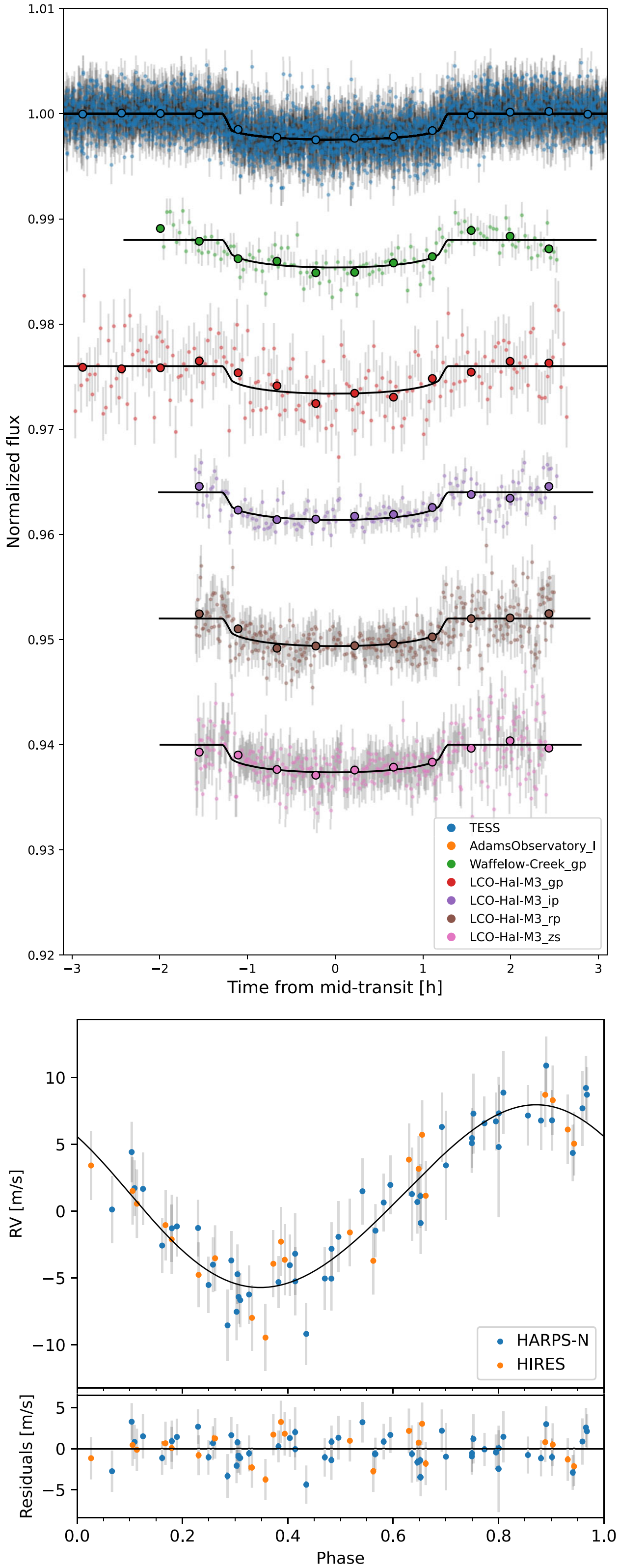

Figure 6. *TESS* and ground-based light curves and binned data (upper), and HARPS-N and HIRES RV data (bottom) for TOI-1472 b, with the 2p + GP model overplotted.

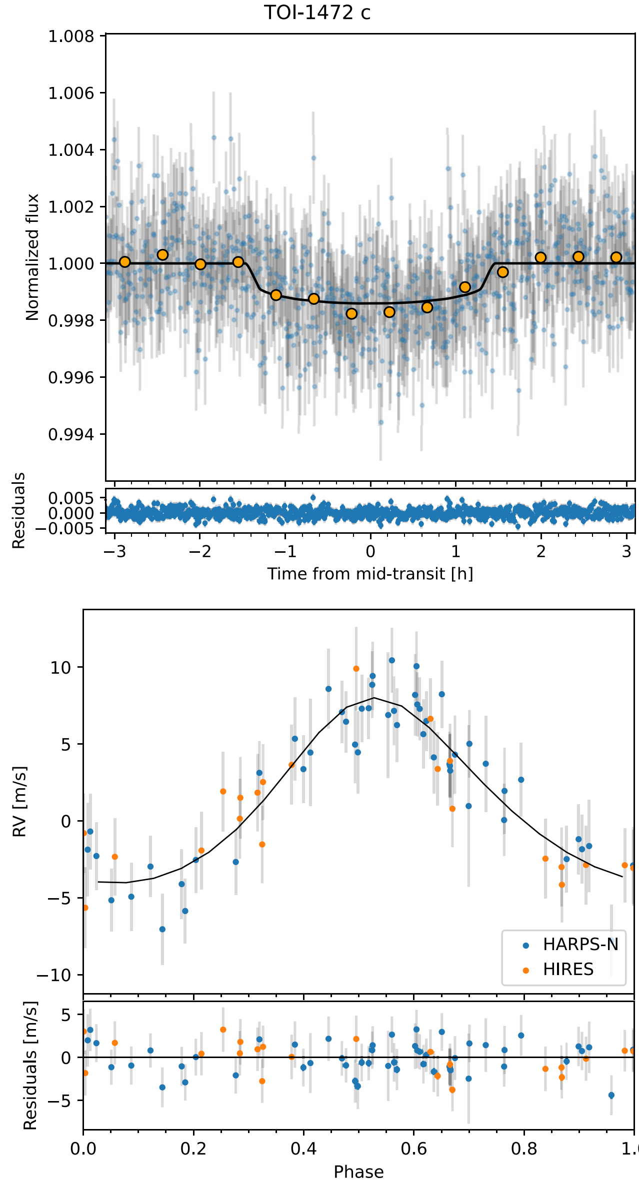

Figure 7. *TESS* light curves and binned data (upper) and HARPS-N and HIRES RV data (bottom) for TOI-1472 c, with the 2p + GP model overplotted.

in the radius measurement is largely due to the availability of additional *TESS* sectors, which provided more transits and better phase coverage, while the improvement in the mass measurement is due to more precise RVs and a larger data set.

TOI-1472 b lies at the external edge of the Neptunian ridge, in the estimated transition between the ridge and savanna (Fig. 10, left). With a density of 1.49 ± 0.13 g cm^{-3}, this planet is compatible with the recently identified population of high-density ridge planets (A. Castro-González et al. 2024b, see Fig. 10, right), which motivated us to perform internal structure and atmospheric evolution simulations (see Section 6.1.1).

We also discovered an additional transiting planet, TOI-1472 c, with an orbital period of 15.54 d, a mass of $21.13^{+0.96}_{-0.99}$ M$_\oplus$, and a radius of 3.334 ± 0.080 R$_\oplus$.

The TOI-1472s planets have measured eccentricities of 0.041 ± 0.002 and 0.172 ± 0.002, respectively. To place the eccentricities of our planets in context, we produced a plot analogous

Table 6. TOI-1648 parameters from the transit and RV joint fit, obtained with the model 1p + GP (one planet plus Gaussian process).

Parameter	Prior[a]	Value[b]
Model parameters		
Orbital period $P_{\rm orb}$ (d)	$\mathcal{U}[6.8, 7.8]$	$7.331602^{+0.000015}_{-0.000020}$
Transit epoch T_0 (BJD – 245 0000)	$\mathcal{U}[9925.1, 9925.5]$	$9925.3431^{+0.0008}_{-0.0010}$
$\sqrt{e}\sin\omega_\star$	$\mathcal{U}(-1, 1)$	0.11 ± 0.18
$\sqrt{e}\cos\omega_\star$	$\mathcal{U}(-1, 1)$	$-0.380^{+0.092}_{-0.070}$
Scaled planetary radius $R_{\rm p}/R_\star$	$\mathcal{U}[0, 0.5]$	$0.0287^{+0.0015}_{-0.0011}$
Impact parameter, b	$\mathcal{U}[0, 1]$	$0.736^{+0.067}_{-0.060}$
RV semi-amplitude variation K (m s^{-1})	$\mathcal{U}[0, 50]$	$2.83^{+0.38}_{-0.47}$
Derived parameters		
Planet radius ($R_{\rm J}$)	...	$0.227^{+0.013}_{-0.011}$
Planet radius ($R_\oplus$)	...	$2.54^{+0.14}_{-0.12}$
Planet mass ($M_{\rm J}$)	...	$0.0233^{+0.0035}_{-0.0040}$
Planet mass ($M_\oplus$)	...	$7.4^{+1.1}_{-1.3}$
Eccentricity e	...	$0.178^{+0.075}_{-0.053}$
Scaled semimajor axis $a/R_\star$	...	$26.4^{+0.6}_{-1.9}$
Semimajor axis a (au)	...	$0.0694^{+0.0016}_{-0.0017}$
$\omega_{\rm P}$ (°)	...	286^{+7}_{-6}
Orbital inclination i (°)	...	$88.29^{+0.11}_{-0.26}$
Transit duration T_{41} (d)	...	$0.0642^{+0.0055}_{-0.0048}$
Transit duration T_{32} (d)	...	$0.0566^{+0.0058}_{-0.0063}$
Calculated parameters		
Equilibrium temperature[c] $T_{\rm eq}$ (K)		799 ± 16
Planetary density $\rho_{\rm P}$ (g cm^{-3})		2.49 ± 0.60
Other system parameters		
Jitter term $\sigma_{\rm HARPS\text{-}N}$ (m s^{-1})	$\mathcal{U}[0, 60]$	$0.65^{+0.57}_{-0.40}$
Limb darkening q_1	$\mathcal{N}[0.5239, 0.1]$	0.53 ± 0.1
Limb darkening q_2	$\mathcal{N}[0.0985, 0.1]$	$0.107^{+0.099}_{-0.096}$
Stellar activity GP model parameters		
$h_{\rm HARPS\text{-}N}$ (m s^{-1})	$\mathcal{U}[0, 100]$	$2.27^{+0.47}_{-0.34}$
λ (d)	$\mathcal{U}[5, 2000]$ 706^{+392}_{-210}	
ω	$\mathcal{U}[0.01, 0.60]$ $0.085^{+0.022}_{-0.019}$	
θ ($P_{\rm rot}$) (d)	$\mathcal{U}[2, 100]$	31.8^{+32}_{-7} [d]

[a] $\mathcal{U}[a, b]$ refers to uniform priors between a and b, $\mathcal{N}[a, b]$ to Gaussian priors with median a and standard deviation b.
[b] Parameter estimates and corresponding uncertainties are defined as the median and the 16th and 84th percentiles of the posterior distributions.
[c] $T_{\rm eq} = T_\star\,(R_\star/2a)^{1/2}\,[f(1 - A_{\rm B})]^{1/4}$, assuming efficient recirculation $f = 1$ and a null Bond albedo ($A_{\rm B} = 0$).
[d] The posterior distribution exhibits a double peak: one around 32 d and another around 64 d. When the prior range is extended to 200 d, an additional peak appears near 160 d (five times 32 d).

to fig. 1 in A. C. M. Correia, V. Bourrier & J. B. Delisle (2020), showing eccentricity as a function of orbital period for the population of super-Earths and sub-Neptunes (Fig. 11). On this diagram, we overplotted our three planets – TOI-1472 b, TOI-1472 c, and TOI-1648 b (see Section 6.2) – highlighting how their eccentricities compare to the broader sample.

TOI-1472 b's low eccentricity lies below the typical eccentricity ($e \sim 0.15$) observed for warm Neptunes (A. C. M. Correia et al. 2020), suggesting that tidal circularization has played a significant role at its relatively short orbital period. This is consistent with theoretical expectations where the tidal circularization time-scale scales steeply with orbital period as $\tau_{\rm circ} \propto P_{\rm orb}^{13/3}$, leading to more efficient damping at shorter periods. In contrast, TOI-1472 c exhibits a higher eccentricity, close to the median value found in A. C. M. Correia et al. (2020)'s sample. Its longer orbital period implies weaker tidal damping, allowing eccentricity to persist over long time-scales. This elevated eccentricity may be maintained by mechanisms such as secular excitation from other companions or atmospheric processes that delay circularization, as discussed by A. C. M. Correia et al. (2020). Together, the differing eccentricities of the two planets highlight a system where tidal effects effectively damp eccentricity for the inner planet but are less efficient for the outer one, consistent with the broader trends illustrated in fig. 1 of A. C. M. Correia et al. (2020).

6.1.1 *Internal structure and atmospheric evolution for TOI-1472 b*

We modelled the internal structure and atmospheric evolution of TOI-1472 b using the JADE code.[10] This framework allows us to place constraints on the planet's current interior composition and estimate its mass at the time of protoplanetary disc dispersal.

JADE uses a Markov chain Monte Carlo (MCMC) approach to infer key structural parameters of the planet – namely, the fraction of the total mass attributed to the silicate mantle, to the gaseous envelope, and the envelope's metallicity. The retrieval is informed by the measured planetary mass and radius (Table 5) and the stellar age

[10] Version 1.0.0, available at https://gitlab.unige.ch/spice_dune/jade.

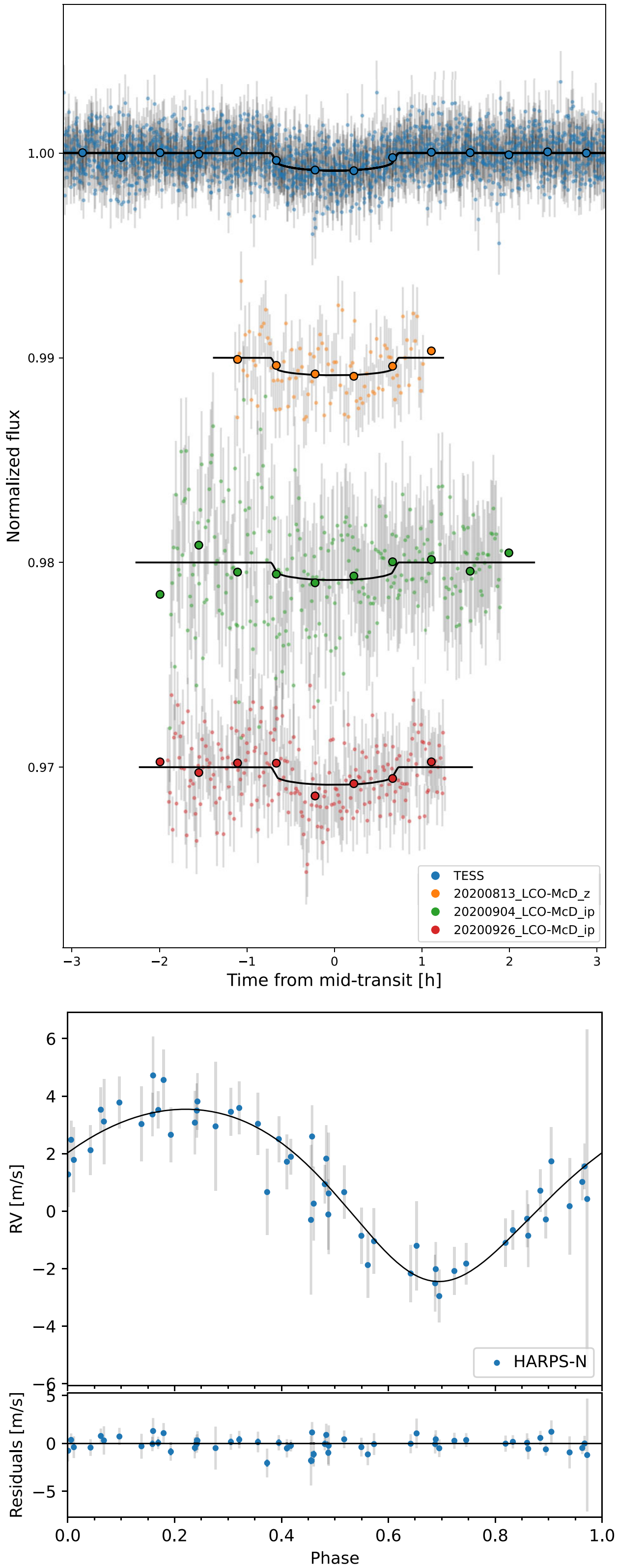

Figure 8. *TESS* and ground-based light curves and binned data (upper) and HARPS-N RV data (bottom) for TOI-1648 b, with the 1p + GP model overplotted.

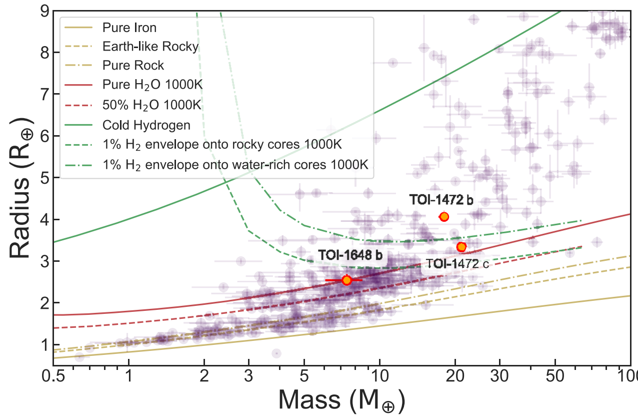

Figure 9. Mass–radius diagram for known exoplanets with measured masses and radii with precision better than 30 per cent. The theoretical composition models from L. Zeng, D. D. Sasselov & S. B. Jacobsen (2016) are shown (solid and dashed curves). Our planets, TOI-1472 b, TOI-1472 c, and TOI-1648 b, are overplotted in colour.

derived in Section 3.1, while also accounting for stellar irradiation [including X-ray and extreme ultraviolet (XUV)] and internal heat from the planet's core.

The planet is modelled with a layered interior structure, consisting of an iron core, a silicate mantle, and an overlying hydrogen–helium envelope. The helium mass fraction is set to $Y = 0.2$, consistent with the composition of Neptune (W. B. Hubbard, M. Podolak & D. J. Stevenson 1995; R. Helled, N. Nettelmann & T. Guillot 2020). The envelope includes a radiative upper layer and a deeper convective zone. Envelope opacities are adjusted by including trace metallic elements with solar abundances, parametrized by a metallicity term ($Z_{\rm met}$). The internal structure is calculated by integrating from the top of the atmosphere inward using a one-dimensional thermal model and polytropic equations of state for the rocky layers (S. Seager et al. 2007), iterating until the integrated mass reaches zero at the core (e.g. E. D. Lopez & J. J. Fortney 2013; S. Jin et al. 2014).

To account for the uncertainty in stellar age, we ran three separate retrievals using the nominal age (4.1 Gyr) and its $\pm 3\sigma$ bounds. Each run consisted of 30 000 MCMC steps with 30 walkers and a burn-in phase of 6000 steps. The retrieved internal parameters showed consistency across age ranges within their 1σ uncertainties, so we adopt the results from the nominal-age run, reported in Table 5.

Following the internal structure modelling, we simulated the long-term atmospheric evolution. We fixed the mantle and core mass fractions, and adopted a small non-zero envelope metallicity ($Z_{\rm met} \sim 0.04$) inferred from the previous step. This small value ensures a physically realistic envelope structure without significantly affecting the model outcome (see M. Attia et al. 2025).

Unlike scenarios involving late high-eccentricity migration – which allow planets to temporarily avoid high stellar irradiation and delay atmospheric loss (M. Attia et al. 2021, 2025) – we assume TOI-1472 b underwent early disc-driven migration. In this case, the planet settled near its current close-in orbit early in its evolution, experiencing prolonged and intense stellar irradiation. This assumption places the planet in a configuration that maximizes its exposure to atmospheric erosion, enabling us to estimate its maximum initial mass. Stellar bolometric and high-energy (XUV) luminosity histories were computed with the GENEC stellar evolution models (P. Eggenberger et al. 2008), to capture how changing irradiation shaped the planet's atmospheric evolution.

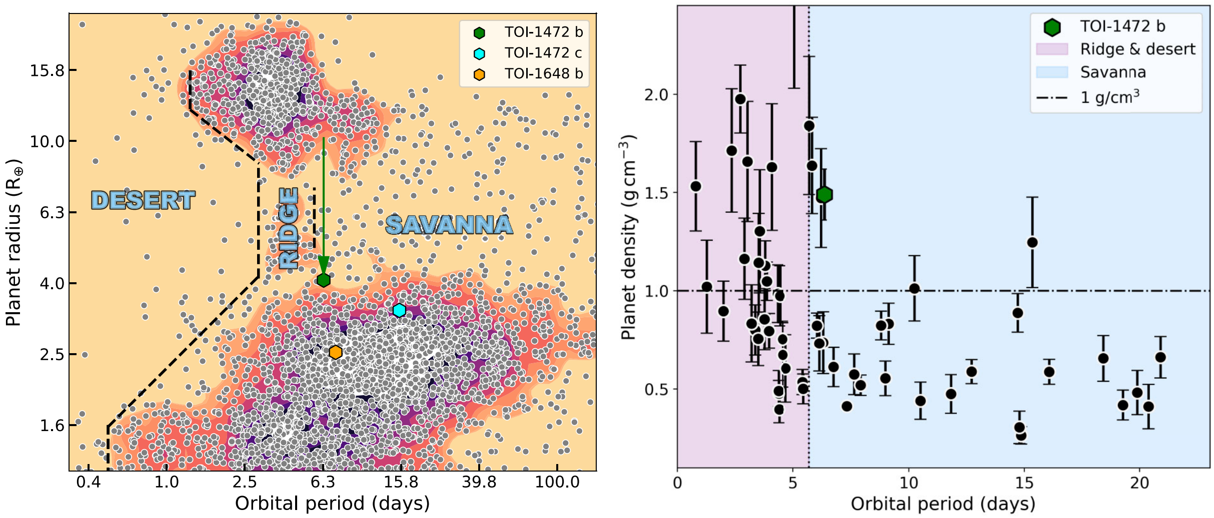

Figure 10. Left: Planet radius versus orbital period for all known exoplanets, highlighting the Neptunian desert, ridge, and savanna derived by A. Castro-González et al. (2024a). The arrows represent the evolution of TOI-1472 b radius from the initial value to the current value. Right: Density–period diagram of all Neptunian planets (4.5 and 8.5 $R_\oplus$) with density precision better than 33 per cent, with TOI-1472 b overplotted. These plots were generated with NEP-DES (https://github.com/castro-gzlz/nep-des).

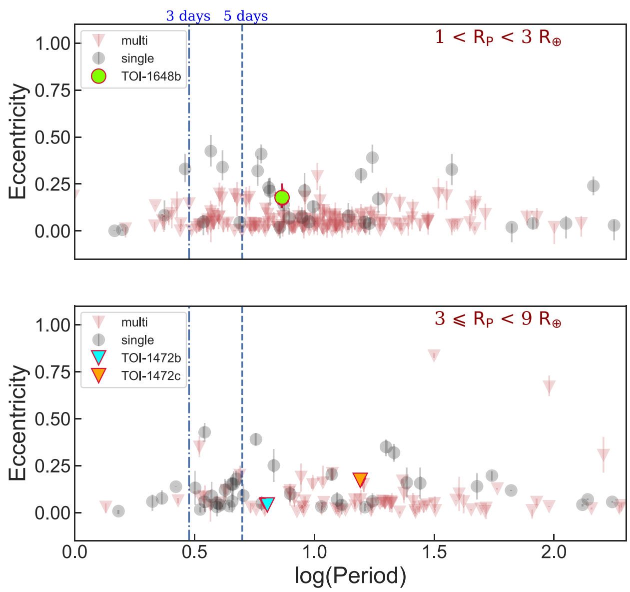

Figure 11. Distribution of eccentricities as a function of the orbital period for Earth-sized planets (upper) and Neptune-sized planets (bottom). The dashed blue lines represent the 3- and 5-d boundaries. The red triangles represent the planets in multiplanetary systems. Data taken as of 2025 June.

Under this early migration assumption, we held the planet's orbital configuration constant and switched off dynamical evolution in the JADE runs. The simulations began at the expected time of disc dispersal and extended to 13 Gyr, encompassing the full plausible age range of the system within 3σ. These simulations trace the mass and radius evolution of the planetary envelope over time, enabling us to infer the maximum initial mass the planet could have had while still matching present-day observations.

We initialized a series of simulations with increasing masses, starting from the observed value of 0.06 M_J up to 1 M_J. For each case, the planet's radius at the system's current age was compared

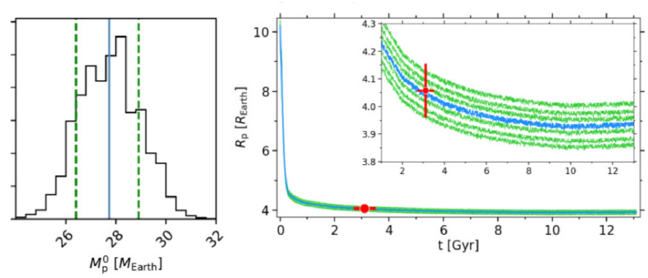

Figure 12. JADE simulations of atmospheric evolution for TOI-1472 b. Left: Posterior probability distribution for the planet's initial mass. The median value is indicated by a solid blue line, while the dashed green lines mark the 1σ highest density interval (HDI). Right: Time evolution of the planet's radius from the best-fitting simulation (blue) alongside a selection of representative models within the 1σ HDI (green). The observed planetary radius and system age, including their uncertainties, are shown as a red data point. The inset provides a closer view of the radius evolution over a more limited time range.

to the observed radius. Using importance sampling, we constructed a posterior distribution of initial masses, adopting the median and highest density interval as the best-fitting value and uncertainty (see Fig. 12, left panels). This estimate represents the maximum feasible initial mass – any higher mass would retain too much atmosphere under the assumed high-irradiation conditions and yield a planet larger than observed, making it incompatible with current measurements.

Fig. 12 illustrates the atmospheric evolution history of TOI-1472 b under the assumption that it migrated early to its current close-in orbit. During the first few hundred million years – when the host star's XUV emission was at its peak – the planet experienced substantial atmospheric erosion. As stellar high-energy output declined over time, the rate of atmospheric escape decreased, leading to a gradual contraction of the planetary radius over several gigayears.

We carried out atmospheric evolution simulations for a range of initial planetary masses, from 0.06 to 1.0 M_J, keeping all other planetary parameters constant. The simulation that best matches the observed radius (depicted as the blue curve in the right panel of Fig.

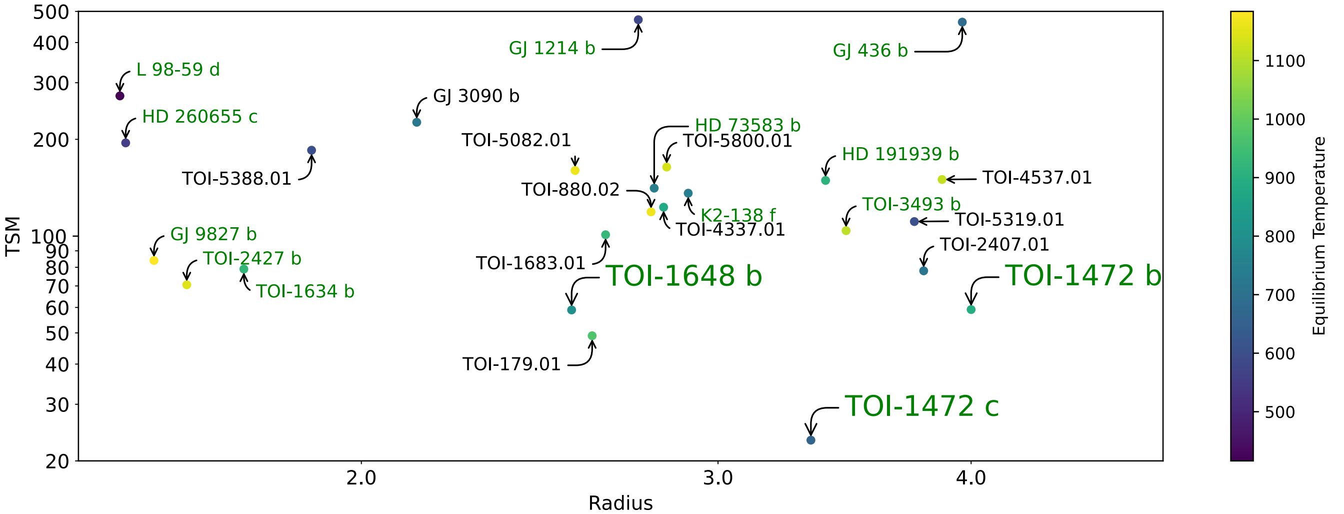

Figure 13. TSM versus planet radius for hot ($350 < T_{\rm eq} < 1250$ K) small sub-Neptunes ($1.50 < R_{\rm p} < 2.75$ $R_\oplus$) and large sub-Neptunes ($2.75 < R_{\rm p} < 4.00$ $R_\oplus$). Data come from B. J. Hord et al. (2024) and include planets with high TSM and mass determination above 5σ recently confirmed by P. Chaturvedi et al. (2025, TOI-3439 b) and H. Schmerling et al. (2025, TOI-2427 b). Names of the confirmed planets with mass measurements >5σ are in green. Planets presented in this paper are annotated with larger fonts.

12) indicates that, at an estimated system age of 3 Gyr, TOI-1472 b is likely still undergoing atmospheric loss, with its radius continuing to decrease below its current observed size of approximately 4 $R_\oplus$. Under the assumption of early, rapid inward migration – which maximizes mass loss – the planet is inferred to have initially formed with a mass of $27.7 \pm 1.2\,M_\oplus$ (equivalent to 0.087 $M_{\rm J}$) and a radius of about 10.2 $R_\oplus$. In this scenario, the envelope mass was around $10.7\,M_\oplus$, or roughly 39 per cent of the total mass. We note that the uncertainty on this initial mass primarily reflects the system age under this migration assumption; different migration histories would likely lead to larger variations than indicated by this error. The left panel of Fig. 10 shows the planet's current location and its inferred evolutionary track from its initial, larger radius to its present-day size.

Following E. M. R. Kempton et al. (2018), we calculated the transmission spectroscopy metric (TSM) and the emission spectroscopy metric (ESM) for the planets of TOI-1472. For these calculations, we used stellar parameters ($R_\star$ and $T_{\rm eff}$) from Table 4 (BACCHUS + PARAM), photometric and kinematic data (m_J, m_K, and RV) from Table 1, and planetary parameters ($R_{\rm p}$, $M_{\rm p}$, and $T_{\rm eq}$) from Table 5.

Fig. 13 displays all the sub-Neptunes (with radius $\leq$4 $R_\oplus$) and their TSM values, with overplotted the planets from this work. The TSM values are 59.1 $\pm$ 6.0 and 23.2 $\pm$ 2.3 for TOI-1472 b and TOI-1472 c, respectively. The ESM is 8.8 $\pm$ 0.6 for TOI-1472 b, and 2.8 $\pm$ 0.2 for TOI-1472 c. The TSM and ESM of TOI-1472 b are favourable for *James Webb Space Telescope* (*JWST*) follow-up observations. Unfortunately, those of TOI-1472 c are too low.

For TOI-1472 b, three RV measurements were obtained during transit. Although these in-transit data are not analysed in this work, they present a valuable opportunity for future studies. In-transit RVs can be used to probe atmospheric escape, particularly of species like hydrogen and helium, through high-resolution transmission spectroscopy. Additionally, such measurements are influenced by the Rossiter–McLaughlin (RM) effect, which for TOI-1472 b is expected to produce a semi-amplitude of approximately 3.9 m s^{-1}. Targeted observations of the RM effect could help constrain the projected spin–orbit alignment, offering further insight into the system's formation and migration history.

6.1.2 Dynamical analysis of TOI-1472 system

To ascertain the dynamical stability of the solution presented in Table 5, we employed the reversibility error method (REM; F. Panichi, K. Goździewski & G. Turchetti 2017), which has been demonstrated to be a close analogue of the maximum Lyapunov exponent. In the analysis of multibody systems it relies on numerical integration schemes that are time reversible, in particular symplectic algorithms. This method is based on calculating the difference between the initial state vector and the final state vector, which is obtained by integrating the system of equations at a specific time and returning to the initial epoch. The difference thus defined will depend on the dynamic nature of the system. $\widehat{\rm REM} = 1$ or $\log \widehat{\rm REM} = 0$ means that the difference reaches the size of the orbit.

The dynamical stability of the solution was tested using the `whfast` integrator with the 17th order corrector (with a fixed time-step of 0.15 d) as implemented within the REBOUND package (H. Rein & S. F. Liu 2012; H. Rein & D. Tamayo 2015; H. Rein, D. Tamayo & G. Brown 2019) for $\simeq 2 \times 10^5$ orbital periods of the outermost planet ($\simeq$8500 yr). As illustrated in Fig. 14, we obtained $\log \widehat{\rm REM} \leq -5$, indicating that the solution and its surrounding area are stable. The $\pm 3\sigma$ uncertainty of the orbital period and eccentricity of the TOI-1472 c, placed on the dynamical maps, shows a safe distance from the chaotic structures.

We identified several mean motion resonances (MMRs) within the examined orbital period and eccentricity parameter space of TOI-1472 c, as illustrated in Fig. 14. Using the `ias15` integrator from the REBOUND package (H. Rein & D. S. Spiegel 2015), we computed the temporal evolution of critical angles for each resonance. Fig. 15 presents representative examples of the 5:2 MMR and 12:5 MMR, where the upper panels demonstrate libration of the critical angles, confirming the resonant character of the investigated solutions. The ranges of $P_{\rm c}$ and $e_{\rm c}$ parameter values explored in these tests extend well beyond the 3σ range. The nominal set of initial conditions for the TOI-1472 system listed in Table 5 corresponds to a non-resonant solution.

The dominance of the number of stable over unstable solutions in the study area (Fig. 14) results in faster calculations using the REM factor compared to the popular Mean Exponential Growth factor of

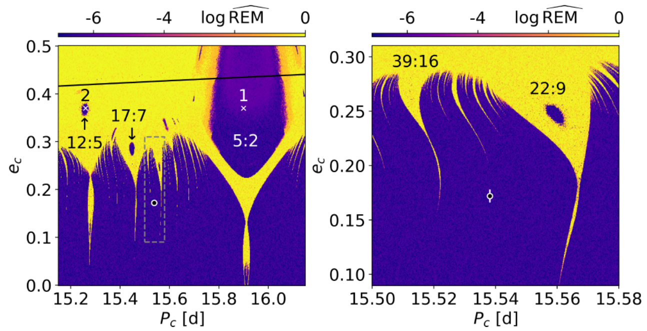

Figure 14. Dynamical maps for a wide range of orbital periods and eccentricities of the TOI-1472 c (the right panel is a zoomed version of the left plot). Small values of the fast indicator log $\widehat{\text{REM}}$ characterize regular (long-term stable) solutions, which are marked with black/dark blue colour. Chaotic solutions are marked with brighter colours, up to yellow. The black line represents the so-called collision curve of orbits, defined by the condition: $a_b(1 + e_b) = a_c(1 - e_c)$. The black filled circle with a white rim indicates the position of the solution for the outer planet TOI-1472 c presented in Table 5. Numbers show identified high-order resonances. Points 1 and 2 refer to Fig. 15. The resolution for the plots is 601 × 301 points.

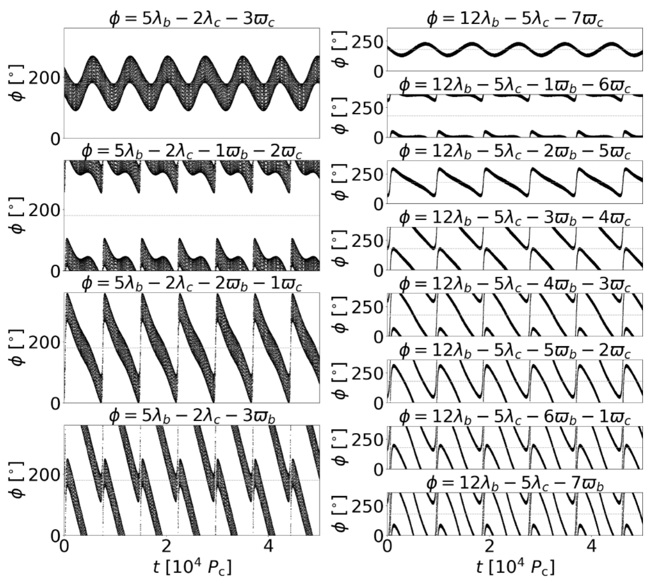

Figure 15. Evolution of critical angles for selected orbital period and eccentricity values of TOI-1472 c, corresponding to the points marked in Fig. 14. The remaining orbital elements are adopted from Table 5. The left column shows the 5:2 MMR (point 1: $P_c = 15.9$ d, $e_c = 0.37$), while the right column shows the 12:5 MMR (point 2: $P_c = 15.26$ d, $e_c = 0.37$).

Nearby Orbits (MEGNO; F. Panichi et al. 2017). CPU time can be at least doubled by using the MEGNO method. The application of the REM method for the TOI-1472 is therefore justified.

Due to gravitational interactions between the planets in the TOI-1472 system, arising from their close proximity and non-zero eccentricities, we evaluated the transit timing variation (TTV) amplitude. For these calculations, we again employed the `ias15` integrator from the REBOUND package. The results presented in Fig. 16, displayed in the eccentricity space of both planets, were computed over ∼300 transits for TOI-1472 b and ∼120 transits for TOI-1472 c, spanning the temporal coverage of *TESS* photometric observations from Sector 17 to Sector 85. The TTV amplitudes obtained for the

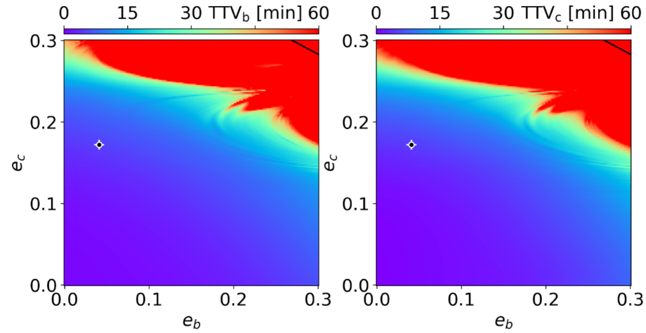

Figure 16. TTV amplitude in the (e_b, e_c)-plane calculated over the temporal span of the TOI-1472 photometric data. The black filled circle with a white rim shows the location of the solution from our modelling (Table 5). The error bars represent 3σ uncertainties.

nominal solution given in Table 5 reach ∼5 min, making them nearly undetectable with the available photometric precision.

6.2 TOI-1648 b

We find TOI-1648 b to have a slightly eccentric orbit with a period of ∼7.33 d, and we measure a mass of $7.4^{+1.1}_{-1.3}$ $M_\oplus$ and a radius of $2.54^{+0.14}_{-0.12}$ $R_\oplus$ (Table 6 and Fig. 9). TOI-1648 b belongs to the group of small sub-Neptunes defined by E. M. R. Kempton et al. (2018) as planets with radii between 1.5 and 2.75 $R_\oplus$. Recently, B. J. Hord et al. (2024) presented a sample of *TESS* planets and planet candidates optimal for transmission and emission spectroscopy with *JWST* in a given range of planetary sizes and equilibrium temperatures. With $T_{eq} = 799 \pm 16$ K, TOI-1648 b lies exactly at the boundary of two of the equilibrium temperature ranges defined by B. J. Hord et al. (2024) between 350 and 800 K and between 800 and 1250 K. Therefore, we have plotted all *TESS* small sub-Neptune planets and planetary candidates from the two above-mentioned equilibrium temperature groups in Fig. 13. With TSM = 58.9 ± 14.5 TOI-1648 b ranks sixth in the group of small sub-Neptunes with equilibrium temperatures between 350 and 1250 K and mass determination >5σ. With the value of 5.0 ± 0.6 of the ESM, TOI-1648 b is also suitable for atmospheric characterization with the emission spectroscopy.

TOI-1648 b presents a relatively high eccentricity of $0.178^{+0.075}_{-0.053}$ (Fig. 11, upper panel). This suggests that tidal circularization alone cannot fully explain its current orbital configuration (assuming that the planet moved inward during the early stages of the system's formation). Possible explanations include interactions with distant companions, which could maintain or excite its eccentricity via secular perturbations, as proposed in the companion-driven excitation scenario. Alternatively, atmospheric tides or sustained atmospheric evaporation could delay orbital circularization (J. E. Owen & D. Lai 2018). Thus, TOI-1648 b may exemplify a system where tidal damping has not yet circularized the orbit, aligning with A. C. M. Correia et al. (2020)'s observation that some warm Neptunes retain moderate eccentricities even after billions of years.

6.3 Mass–radius diagram

The three planets in our sample occupy distinct positions on the mass–radius diagram (Fig. 9), highlighting a diversity of internal structures and atmospheric outcomes. TOI-1648 b (2.5 $R_\oplus$, 7.4 $M_\oplus$) lies directly on the pure-H_2O composition curve from L. Zeng et al. (2016), consistent with a volatile-rich interior and little to no H/He envelope. Its bulk density of ∼2.6 g cm^{-3} disfavours a rocky super-

Earth interpretation and instead points to an ice-dominated planet that has either lost its primordial atmosphere or failed to accrete one of significant size. TOI-1472 c (3.33 $R_\oplus$, 21.1 $M_\oplus$) is located slightly above the pure-H_2O line, indicating the presence of a modest H/He layer atop a water-rich core. Its density of $\sim$3.2 g cm^{-3} suggests that this envelope constitutes only a small fraction of the total planetary mass. By contrast, TOI-1472 b (4.06 $R_\oplus$, 18.1 $M_\oplus$) lies well above the 1 per cent H/He on water-rich core track, implying a more extended gaseous envelope and a substantially lower density of $\sim$1.5 g cm^{-3}.

These structural inferences are consistent with our atmospheric evolution simulations. For TOI-1472 b, JADE modelling under the assumption of early disc-driven migration shows that the planet likely formed with an initial mass of 27.7 $\pm$ 1.2 $M_\oplus$ and an envelope comprising $\sim$39 per cent of its mass. The model further predicts that the planet remains in a state of ongoing atmospheric escape, with its radius still contracting from an initially inflated $\sim$10.2 $R_\oplus$. This explains its present-day position above the 1 per cent H/He envelope curve. TOI-1472 c, by contrast, is consistent with a history of more efficient atmospheric loss, leaving behind only a thin gaseous layer. Meanwhile, TOI-1648 b's alignment with the pure-H_2O track implies that it is either an almost atmosphere-free water world or has retained only a negligible volatile component after prolonged erosion on its short-period orbit.

Taken together, the three planets trace an evolutionary sequence across the sub-Neptune regime: from a nearly atmosphere-free water world (TOI-1648 b), to a water-rich planet with a tenuous H/He veneer (TOI-1472 c), to a volatile-rich sub-Neptune still undergoing mass loss (TOI-1472 b). Their relative positions in mass–radius space emphasize how small differences in early envelope accretion and irradiation history can drive divergent present-day outcomes in bulk density and atmospheric observability.

7 CONCLUSIONS

As part of the KESPRINT collaboration, we have presented a comprehensive characterization of three transiting planets identified by *TESS*, combining precise RV measurements and transit modelling to refine their fundamental parameters and investigate their internal structure, atmospheric evolution, and dynamical stability.

We provide an improved mass measurement and detailed analysis of the previously known (A. S. Polanski et al. 2024) warm sub-Neptune TOI-1472 b (4.06 $R_\oplus$, 18.1 $M_\oplus$), which orbits a G-type star with a period of 9.2 d. Our analysis places it at the outer edge of the Neptunian ridge and near the transition into the Neptunian savanna – an underpopulated region in radius–period–density space. The combination of low density and its location near this transitional zone makes it a compelling target for atmospheric evolution modelling. Using internal structure and evolutionary simulations, we infer that TOI-1472 b likely formed with a significantly larger radius and envelope mass fraction ($\sim$39 per cent), and has since undergone substantial atmospheric loss due to early and prolonged exposure to high stellar irradiation. Our forward modelling suggests the planet is still losing atmosphere and evolving towards a smaller radius.

In addition to refining the parameters of TOI-1472 b, we discovered a second planet in the system, TOI-1472 c, with a mass of 21.1 $M_\oplus$, a radius of 3.33 $R_\oplus$, and a slightly eccentric orbit (e = 0.172). We performed a dynamical stability analysis and confirmed that the two-planet configuration is long-term stable and dynamically non-resonant. If both planets formed simultaneously in the protoplanetary disc and migrated inward, one would expect near-circular, approximately resonant orbits and a lower density for the outer planet because of reduced irradiation. Instead, TOI-1472 c appears unusually dense and on an eccentric, non-resonant orbit. This combination suggests a different evolutionary pathway – for example, one or more giant impacts could increase the planet's density and excite its eccentricity, producing the observed departure from resonance. High-eccentricity migration, however, is unlikely for TOI-1472 c, given its small radius and relatively large semimajor axis.

Among the two planets, TOI-1472 b emerges as an excellent target for atmospheric characterization, with both TSM and ESM values that favour future *JWST* transmission and emission spectroscopy.

We also present the discovery and characterization of TOI-1648 b, a 2.5 $R_\oplus$, 7.4 $M_\oplus$ sub-Neptune on a 7.3-d orbit, which lies at the temperature boundary between two key *JWST* spectroscopic windows. Its favourable TSM (58.9) and ESM (5.0) place it among the most promising small warm sub-Neptunes accessible for transmission and emission spectroscopy, especially among those with high-significance mass measurements. This makes TOI-1648 b a valuable addition to the sample of well-characterized planets suitable for comparative atmospheric studies.

Together, these planets enrich the diversity of known sub-Neptunes and offer key test cases for models of planetary structure, migration, and atmospheric evolution.

ACKNOWLEDGEMENTS

IC acknowledges financial contribution from the INAF Large Grant 2023 'EXODEMO'. CP gratefully acknowledges the support of the Swedish National Space Agency (DNR 65/19). We acknowledge financial support from the Agencia Estatal de Investigación of the Ministerio de Ciencia e Innovación MCIN/AEI/10.13039/501100011033 and the ERDF 'A way of making Europe' through project PID2021-125627OB-C32, and from the Centre of Excellence 'Severo Ochoa' award to the Instituto de Astrofisica de Canarias. TM acknowledges financial support from the Spanish Ministry of Science and Innovation (MICINN) through the Spanish State Research Agency, under the Severo Ochoa Program 2020–2023 (CEX2019-000920-S) and from the Spanish Ministry of Science and Innovation with the grant no. PID2023-146453NB-100 (*PLAtoSOnG*). HJD acknowledges funding from the same source under grants PID2019-107061GB-C66 and PID2023-149439NB-C41. DRC acknowledges partial support from NASA grant 18-2XRP18_2-0007. This research has made use of the Exoplanet Follow-up Observation Program (ExoFOP; DOI: 10.26134/ExoFOP5) website, which is operated by the California Institute of Technology, under contract with the National Aeronautics and Space Administration under the Exoplanet Exploration Program. Based on observations obtained at the Hale Telescope, Palomar Observatory, as part of a collaborative agreement between the Caltech Optical Observatories and the Jet Propulsion Laboratory operated by Caltech for NASA. The Observatory was made possible by the generous financial support of the W. M. Keck Foundation. The authors wish to recognize and acknowledge the very significant cultural role and reverence that the summit of Maunakea has always had within the Native Hawaiian community. We are most fortunate to have the opportunity to conduct observations from this mountain. GN thanks for the research funding from the Ministry of Science and Higher Education programme, the 'Excellence Initiative – Research University' conducted at the Centre of Excellence in Astrophysics and Astrochemistry of the Nicolaus Copernicus University in Toruń, Poland. DJ, KG, and GN gratefully acknowledge the Centre of Informatics Tricity Academic Supercomputer and networK (CI TASK, Gdańsk, Poland) for computing resources (grant no. PT01016). Some of the observations in this paper made use of the high-resolution imaging instrument `Alopeke and were obtained under Gemini LLP Proposal Number: GN/S-2021A-LP-105. `Alopeke was funded by the NASA Exoplanet Exploration Program and built at the NASA Ames Research Center by Steve B. Howell, Nic Scott, Elliott P. Horch, and Emmett Quigley. `Alopeke was mounted on the Gemini North telescope of the international Gemini Observatory, a program of NSF's OIR Lab, which is managed by the Association of Universities for Research in Astronomy (AURA) under a cooperative agreement with the National Science Foundation on behalf of the Gemini partnership: the National Science Foundation (USA), National Research Council (Canada), Agencia Nacional de Investigación y Desarrollo (Chile), Ministerio de Ciencia, Tecnología e Innovación (Argentina), Ministério da Ciência, Tecnologia, Inovações e Comunicações (Brazil), and Korea Astronomy and Space Science Institute (Korea). JL-B was partially funded by the NextGenerationEU/PRTR grant CNS2023-144309 and national projects PID2019-107061GB-C61 and PID2023-150468NB-I00 by the Spanish Ministry of Science and Innovation/State Agency of Research MCIN/AEI/10.13039/501100011033. Support for this work was provided by NASA through the NASA Hubble Fellowship grant HST-HF2-51559.001-A awarded by the Space Telescope Science Institute, which is operated by the Association of Universities for Research in Astronomy, Inc., for NASA, under contract NAS5-26555. This project has received funding from the European Research Council (ERC) under the European Union's Horizon 2020 Framework Programme (project Spice Dune, grant agreement no. 947634). This work has been carried out in the frame of the National Centre for Competence in Research Planets, supported by the Swiss National Science Foundation (SNSF) under grants 51NF40_182901 and 51NF40_205606. PE acknowledges support from the SNF grant no. 219745. The authors acknowledge support from the Swiss NCCR Planets and the Swiss National Science Foundation. This work has been carried out within the framework of the NCCR Planets, supported by the Swiss National Science Foundation under grants 51NF40182901 and 51NF40205606. JK gratefully acknowledges the support of the Swedish National Space Agency (SNSA; DNR 2020–00104) and of the Swiss National Science Foundation under grant no. TMSGI2_211697. RL acknowledges financial support from the Severo Ochoa grant CEX2021-001131-S funded by MCIN/AEI/10.13039/501100011033 and the European Union (ERC, THIRSTEE, 101164189). Views and opinions expressed are, however, those of the author(s) only and do not necessarily reflect those of the European Union or the European Research Council. Neither the European Union nor the granting authority can be held responsible for them. GM acknowledges financial support from the Severo Ochoa grant CEX2021-001131-S and from the Ramón y Cajal grant RYC2022-037854-I funded by MCIN/AEI/1144 10.13039/501100011033 and FSE+. JIV acknowledges financial support from ANID/Fondo ALMA 2024/No. 31240039 'On the origin of Warm-Giant Planets'. FM acknowledges the financial support from the Agencia Estatal de Investigación del Ministerio de Ciencia, Innovacion y Universidades (MCIU/AEI) through grant PID2023-152906NA-I00.

This work makes use of observations from the LCOGT network. Part of the LCOGT telescope time was granted by NOIRLab through the Mid-Scale Innovations Program (MSIP). MSIP is funded by NSF. This paper is based on observations made with the Las Cumbres Observatory's education network telescopes that were upgraded through generous support from the Gordon and Betty Moore Foundation. Funding for the *TESS* mission is provided by NASA Science Mission Directorate. KAC acknowledges support from the *TESS* mission via subaward s3449 from MIT. This paper is based on observations made with the MuSCAT3 instrument, developed by the Astrobiology Center and under financial support by JSPS KAKENHI (JP18H05439) and JST PRESTO (JPMJPR1775), at Faulkes Telescope North on Maui, HI, operated by the Las Cumbres Observatory.

DATA AVAILABILITY

The data underlying this article are available in the article and in its online supplementary material.

REFERENCES

Aller A., Lillo-Box J., Jones D., Miranda L. F., Barceló Forteza S., 2020, A&A, 635, A128
Ambikasaran S., Foreman-Mackey D., Greengard L., Hogg D. W., O'Neil M., 2015, IEEE Trans. Pattern Anal. Mach. Intell., 38, 252
Attia M., Bourrier V., Eggenberger P., Mordasini C., Beust H., Ehrenreich D., 2021, A&A, 647, A40
Attia M., Bourrier V., Bolmont E., Mignon L., Delisle J.-B., Beust H., Hara N. C., Mordasini C., 2025, A&A, 702, A132
Bean J. L., Raymond S. N., Owen J. E., 2021, J. Geophys. Res.: Planets, 126, e06639
Bellm E. C. et al., 2019, PASP, 131, 018002
Benítez-Llambay P., Masset F., Beaugé C., 2011, A&A, 528, A2
Berger T. A., Huber D., Gaidos E., van Saders J. L., 2018, ApJ, 866, 99
Bourrier V. et al., 2023, A&A, 669, A63
Bressan A., Marigo P., Girardi L., Salasnich B., Dal Cero C., Rubele S., Nanni A., 2012, MNRAS, 427, 127
Brown T. M. et al., 2013, PASP, 125, 1031
Castelli F., Kurucz R. L., 2004, in Piskunov N., Weiss W. W., Gray D. F., eds, Proc. IAU Symp. No. 210, Modelling of Stellar Atmospheres (Poster Contributions). Astron. Soc. Pac., San Francisco, p. A20
Castro-González A. et al., 2022, MNRAS, 509, 1075
Castro-González A. et al., 2023, A&A, 675, A52
Castro-González A., Bourrier V., Lillo-Box J., Delisle J. B., Armstrong D. J., Barrado D., Correia A. C. M., 2024a, A&A, 689, A250
Castro-González A. et al., 2024b, A&A, 691, A233
Chaturvedi P. et al., 2025, A&A, 697, A169
Ciardi D. R., Beichman C. A., Horch E. P., Howell S. B., 2015, ApJ, 805, 16
Collins K., 2019, Am. Astron. Soc. Meeting Abstr., #233, 140.05
Collins K. A., Kielkopf J. F., Stassun K. G., Hessman F. V., 2017, AJ, 153, 77
Correia A. C. M., Bourrier V., Delisle J. B., 2020, A&A, 635, A37
Cosentino R. et al., 2014, in Ramsay S. K., McLean I. S., Takami H., eds, Proc. SPIE Conf. Vol. 9147, Ground-based and Airborne Instrumentation for Astronomy V. SPIE, Bellingham, p. 91478C
Dai F., Masuda K., Winn J. N., Zeng L., 2019, ApJ, 883, 79
de Leon J. P. et al., 2021, MNRAS, 508, 195
Eastman J., Gaudi B. S., Agol E., 2013, PASP, 125, 83
Eggenberger P., Meynet G., Maeder A., Hirschi R., Charbonnel C., Talon S., Ekström S., 2008, Ap&SS, 316, 43
Fulton B. J., Petigura E. A., 2018, AJ, 156, 264
Furlan E., Howell S. B., 2017, AJ, 154, 66
Furlan E., Howell S. B., 2020, ApJ, 898, 47
Furlan E. et al., 2017, AJ, 153, 71
Gaia Collaboration, 2023, A&A, 674, A1
Grunblatt S. K., Howard A. W., Haywood R. D., 2015, ApJ, 808, 127
Gustafsson B., Edvardsson B., Eriksson K., Jørgensen U. G., Nordlund Å., Plez B., 2008, A&A, 486, 951
Hart K. et al., 2023, preprint (arXiv:2304.03791)
Hayes C. R. et al., 2022, ApJS, 262, 34
Helled R., Nettelmann N., Guillot T., 2020, Space Sci. Rev., 216, 38
Hord B. J. et al., 2024, AJ, 167, 233
Hormuth F., Brandner W., Hippler S., Henning T., 2008, J. Phys. Conf. Ser., 131, 012051

Howell S. B., Everett M. E., Sherry W., Horch E., Ciardi D. R., 2011, AJ, 142, 19
Huang C. X. et al., 2020a, Res. Notes Am. Astron. Soc., 4, 204
Huang C. X. et al., 2020b, Res. Notes Am. Astron. Soc., 4, 206
Hubbard W. B., Podolak M., Stevenson D. J., 1995, in Cruikshank D. P., Matthews M. S., Schumann A. M., eds, Neptune and Triton. Univ. Arizona Press, Tucson, AZ, p. 109
Hunter A. A., Macgregor A. B., Szabo T. O., Wellington C. A., Bellgard M. I., 2012, Source Code Biol. Med., 7, 1
Husser T. O., Wende-von Berg S., Dreizler S., Homeier D., Reiners A., Barman T., Hauschildt P. H., 2013, A&A, 553, A6
Ikoma M., Hori Y., 2012, ApJ, 753, 66
Jenkins J. M., 2002, ApJ, 575, 493
Jenkins J. M. et al., 2010, in Radziwill N. M., Bridger A., eds, Proc. SPIE Conf. Vol. 7740, Software and Cyberinfrastructure for Astronomy. SPIE, Bellingham, p. 77400D
Jenkins J. M. et al., 2016, in Chiozzi G., Guzman J. C., eds, Proc. SPIE Conf. Vol. 9913, Software and Cyberinfrastructure for Astronomy IV. SPIE, Bellingham, p. 99133E
Jenkins J. M., Tenenbaum P., Seader S., Burke C. J., McCauliff S. D., Smith J. C., Twicken J. D., Chandrasekaran H., 2020, in Jenkins J. M., ed., Kepler Data Processing Handbook: Transiting Planet Search (Kepler Science Document KSCI-19081-003). NASA Ames Research Center, Moffett Field, CA, p. 9
Jensen E., 2013, Astrophysics Source Code Library, record ascl:1306.007
Jin S., Mordasini C., Parmentier V., van Boekel R., Henning T., Ji J., 2014, ApJ, 795, 65
Johnson D. R. H., Soderblom D. R., 1987, AJ, 93, 864
Kempton E. M. R. et al., 2018, PASP, 130, 114401
Kipping D. M., 2013, MNRAS, 435, 2152
Kochanek C. S. et al., 2017, PASP, 129, 104502
Koposov S. et al., 2022, joshspeagle/dynesty: v2.0.3. Zenodo
Kreidberg L., 2015, PASP, 127, 1161
Lacedelli G. et al., 2021, MNRAS, 501, 4148
Lee E. J., Chiang E., 2016, ApJ, 827, 125
Li J., Tenenbaum P., Twicken J. D., Burke C. J., Jenkins J. M., Quintana E. V., Rowe J. F., Seader S. E., 2019, PASP, 131, 024506
Lillo-Box J., Barrado D., Bouy H., 2012, A&A, 546, A10
Lillo-Box J., Barrado D., Bouy H., 2014, A&A, 566, A103
Lillo-Box J. et al., 2024, A&A, 686, A232
Livingston J. H. et al., 2018a, AJ, 156, 78
Livingston J. H. et al., 2018b, AJ, 156, 277
Lopez E. D., Fortney J. J., 2013, ApJ, 776, 2
Luque R., Pallé E., 2022, Science, 377, 1211
Luque R. et al., 2022, A&A, 664, A199
McCully C., Volgenau N. H., Harbeck D.-R., Lister T. A., Saunders E. S., Turner M. L., Siiverd R. J., Bowman M., 2018, in Guzman J. C., Ibsen J., eds, Proc. SPIE Conf. Vol. 10707, Software and Cyberinfrastructure for Astronomy V. SPIE, Bellingham, p. 107070K
Malavolta L. et al., 2016, A&A, 588, A118
Malavolta L. et al., 2018, AJ, 155, 107
Mamajek E. E., Hillenbrand L. A., 2008, ApJ, 687, 1264
Mandel K., Agol E., 2002, ApJ, 580, L171
Masci F. J. et al., 2019, PASP, 131, 018003
Masseron T., Merle T., Hawkins K., 2016, Astrophysics Source Code Library, record ascl:1605.004
Maxted P. F. L. et al., 2011, PASP, 123, 547
Mayor M. et al., 2011, preprint (arXiv:1109.2497)
Mazeh T., Holczer T., Faigler S., 2016, A&A, 589, A75
Narita N. et al., 2020, in Evans C. J., Bryant J. J., Motohara K., eds, Proc. SPIE Conf. Vol. 11447, Ground-based and Airborne Instrumentation for Astronomy VIII. SPIE, Bellingham, p. 114475K
Owen J. E., Lai D., 2018, MNRAS, 479, 5012
Owen J. E., Wu Y., 2016, ApJ, 817, 107
Palle E. et al., 2023, A&A, 678, A80
Panichi F., Goździewski K., Turchetti G., 2017, MNRAS, 468, 469
Parviainen H., Aigrain S., 2015, MNRAS, 453, 3821
Patel J. A., Espinoza N., 2022, AJ, 163, 228
Polanski A. S. et al., 2024, ApJS, 272, 32
Pollacco D. L. et al., 2006, PASP, 118, 1407
Rein H., Liu S. F., 2012, A&A, 537, A128
Rein H., Spiegel D. S., 2015, MNRAS, 446, 1424
Rein H., Tamayo D., 2015, MNRAS, 452, 376
Rein H., Tamayo D., Brown G., 2019, MNRAS, 489, 4632
Ricker G. R. et al., 2015, J. Astron. Telesc. Instrum. Syst., 1, 014003
Rodrigues T. S. et al., 2017, MNRAS, 467, 1433
Rogers J. G., Schlichting H. E., Owen J. E., 2023, ApJ, 947, L19
Safonov B. S., Lysenko P. A., Dodin A. V., 2017, Astron. Lett., 43, 344
Schlegel D. J., Finkbeiner D. P., Davis M., 1998, ApJ, 500, 525
Schmerling H. et al., 2025, A&A, 699, A185
Scott N. J. et al., 2021, Front. Astron. Space Sci., 8, 138
Seager S., Kuchner M., Hier-Majumder C. A., Militzer B., 2007, ApJ, 669, 1279
Shappee B. J. et al., 2014, ApJ, 788, 48
Smith J. C. et al., 2012, PASP, 124, 1000
Sneden C., 1973, ApJ, 184, 839
Soto M. G., Jenkins J. S., 2018, A&A, 615, A76
Speagle J. S., 2020, MNRAS, 493, 3132
Stassun K. G., Torres G., 2016, AJ, 152, 180
Stassun K. G., Collins K. A., Gaudi B. S., 2017, AJ, 153, 136
Stassun K. G., Corsaro E., Pepper J. A., Gaudi B. S., 2018, AJ, 155, 22
Stumpe M. C. et al., 2012, PASP, 124, 985
Szabó G. M., Kiss L. L., 2011, ApJ, 727, L44
Tayar J., Claytor Z. R., Huber D., van Saders J., 2022, ApJ, 927, 31
Torres G., Andersen J., Giménez A., 2010, A&AR, 18, 67
Twicken J. D., Clarke B. D., Bryson S. T., Tenenbaum P., Wu H., Jenkins J. M., Girouard F., Klaus T. C., 2010, in Radziwill N. M., Bridger A., eds, Proc. SPIE Conf. Vol. 7740, Software and Cyberinfrastructure for Astronomy. SPIE, Bellingham, p. 774023
Twicken J. D. et al., 2018, PASP, 130, 064502
Udry S., Mayor M., Santos N. C., 2003, A&A, 407, 369
Venturini J., Guilera O. M., Haldemann J., Ronco M. P., Mordasini C., 2020, A&A, 643, L1
Vines J. I., Jenkins J. S., 2022, MNRAS, 513, 2719
Wizinowich P. et al., 2000, PASP, 112, 315
Zechmeister M., Kürster M., 2009, A&A, 496, 577
Zechmeister M. et al., 2018, A&A, 609, A12
Zeng L., Sasselov D. D., Jacobsen S. B., 2016, ApJ, 819, 127
Zeng L. et al., 2019, Proc. Natl. Acad. Sci., 116, 9723

APPENDIX A: RV AND ACTIVITY INDICATORS DATA SETS

Table A1. Time series of TOI-1472 from HARPS-N and HIRES data: Julian dates, RVs, S-index, and their related uncertainties. For HARPS-N data the $\log R'_{\rm HK}$ values are listed as well.

	JD	RV (m s^{-1})	$\sigma_{\rm RV}$ (m s^{-1})	S-index	$\sigma_{\rm S\text{-}index}$	$\log R'_{\rm HK}$	$\sigma_{\log R'_{\rm HK}}$
HARPS-N	245 8862.347322	− 14857.16	1.09	0.253	0.004	− 4.83	0.01
	245 8895.370240	− 14848.93	2.07	0.301	0.008	− 4.74	0.01
	245 8896.359494	− 14846.33	1.72	0.284	0.006	− 4.77	0.01
	245 8897.362492	− 14839.18	2.64	0.275	0.007	− 4.78	0.01
	245 8898.360083	− 14839.95	1.71	0.279	0.005	− 4.78	0.01
	245 9132.716760	− 14854.00	1.38	0.279	0.010	− 4.78	0.02
	245 9148.685964	− 14868.38	1.48	0.275	0.006	− 4.78	0.01
	245 9149.517373	− 14874.18	1.62	0.281	0.004	− 4.77	0.01
	245 9150.532833	− 14861.89	1.43	0.286	0.005	− 4.76	0.01
	245 9151.517034	− 14855.56	1.46	0.293	0.012	− 4.75	0.02
	245 9160.502878	− 14855.70	1.20	0.258	0.018	− 4.82	0.04
	245 9204.441437	− 14850.15	1.88	0.262	0.005	− 4.81	0.01
	245 9205.480395	− 14848.11	1.29	0.281	0.012	− 4.77	0.02
	245 9206.451903	− 14852.12	0.99	0.289	0.009	− 4.76	0.02
	245 9248.358036	− 14839.09	1.21	0.302	0.016	− 4.74	0.03
	245 9249.359368	− 14844.27	2.12	0.287	0.009	− 4.76	0.02
	245 9265.334407	− 14851.75	3.06	0.276	0.006	− 4.78	0.01
	245 9268.347483	− 14847.50	1.23	0.279	0.007	− 4.78	0.01
	245 9405.689938	− 14842.43	1.98	0.318	0.011	− 4.71	0.02
	245 9410.640158	− 14859.12	1.64	0.323	0.008	− 4.70	0.01
	245 9432.724961	− 14853.55	1.29	0.312	0.006	− 4.72	0.01
	245 9469.688165	− 14842.09	1.49	0.312	0.007	− 4.72	0.01
	245 9549.505157	− 14854.55	1.43	0.303	0.008	− 4.73	0.01
	245 9572.468757	− 14854.81	1.54	0.301	0.009	− 4.74	0.02
	245 9593.391779	− 14847.19	1.48	0.323	0.008	− 4.70	0.01
	245 9609.368066	− 14846.28	3.73	0.333	0.030	− 4.69	0.05
	245 9610.358438	− 14844.42	1.50	0.314	0.009	− 4.72	0.01
	245 9765.638588	− 14852.24	1.19	0.308	0.006	− 4.72	0.01
	245 9766.632046	− 14855.66	1.92	0.306	0.012	− 4.73	0.02
	245 9785.657277	− 14862.89	1.57	0.311	0.009	− 4.72	0.01
	245 9810.618441	− 14850.64	1.41	0.322	0.007	− 4.70	0.01
	245 9811.612679	− 14851.81	1.72	0.323	0.009	− 4.70	0.01
	245 9812.650632	− 14849.92	1.67	0.322	0.009	− 4.70	0.01
	245 9813.633064	− 14848.98	4.99	0.338	0.038	− 4.68	0.06
	245 9814.644726	− 14848.58	2.26	0.317	0.014	− 4.71	0.02
	245 9882.688144	− 14860.05	1.61	0.312	0.010	− 4.72	0.02
	245 9883.631847	− 14850.99	1.33	0.296	0.007	− 4.75	0.01
	245 9888.505341	− 14844.75	1.08	0.314	0.005	− 4.72	0.01
	245 9888.605016	− 14842.50	1.38	0.319	0.007	− 4.71	0.01
	245 9890.567454	− 14834.69	1.40	0.325	0.007	− 4.70	0.01
	245 9911.499567	− 14860.87	1.88	0.293	0.011	− 4.75	0.02
	245 9912.325684	− 14866.14	1.17	0.291	0.006	− 4.75	0.01
	245 9913.428690	− 14860.74	1.08	0.315	0.005	− 4.71	0.01
	245 9931.372061	− 14863.51	1.32	0.333	0.007	− 4.69	0.01
	245 9934.365966	− 14841.16	1.13	0.300	0.005	− 4.74	0.01
	245 9936.468371	− 14843.89	1.52	0.296	0.009	− 4.75	0.01
	245 9937.396886	− 14856.30	1.28	0.287	0.006	− 4.76	0.01
	245 9950.353060	− 14860.33	2.08	0.311	0.013	− 4.72	0.02
	245 9958.345769	− 14857.41	1.81	0.347	0.011	− 4.66	0.02
	245 9972.412831	− 14849.02	2.48	0.311	0.017	− 4.72	0.03
	245 9989.349576	− 14861.51	2.55	0.340	0.018	− 4.67	0.03
	246 0259.580937	− 14846.58	1.43	0.320	0.008	− 4.71	0.01
HIRES	245 9071.110466	− 1.98	1.71	0.245	0.001		
	245 9093.055865	− 6.64	1.66	0.236	0.001		
	245 9117.044165	− 15.61	1.54	0.258	0.001		
	245 9119.057556	− 5.17	1.58	0.253	0.001		
	245 9119.099490	− 2.61	1.74	0.244	0.001		
	245 9119.142826	− 7.16	1.80	0.235	0.001		
	245 9188.937172	14.56	1.93	0.256	0.001		
	245 9232.768015	1.07	1.65	0.238	0.001		
	245 9268.720687	7.62	1.80	0.230	0.001		

Table A1 – *continued*

JD	RV (m s^{-1})	σ_{RV} (m s^{-1})	S-index	$\sigma_{S\text{-index}}$	$\log R'_{HK}$	$\sigma_{\log R'_{HK}}$
245 9378.106313	− 8.99	1.62	0.270	0.001		
245 9409.115634	− 3.24	1.50	0.306	0.001		
245 9445.118985	4.82	1.48	0.285	0.001		
245 9470.920928	8.93	1.42	0.279	0.001		
245 9497.877869	0.10	1.76	0.260	0.001		
245 9511.970049	− 6.42	1.85	0.288	0.001		
245 9541.949301	− 2.15	1.65	0.266	0.001		
245 9574.762635	1.26	1.55	0.270	0.001		
245 9598.718018	3.48	1.73	0.280	0.001		
245 9632.736802	− 7.05	1.64	0.272	0.001		
245 9738.107008	3.89	1.76	0.291	0.001		
245 9760.096365	2.70	1.75	0.297	0.001		
245 9776.105728	8.93	1.76	0.295	0.001		

Table A2. Time series of additional TOI-1472 activity indicators from HARPS-N DRS: bisector, CCF contrast, CCF FWHM, and their related uncertainties.

JD	BIS (m s^{-1})	σ_{BIS} (m s^{-1})	CONT (km s^{-1})	σ_{CONT} (km s^{-1})	FWHM (km s^{-1})	σ_{FWHM} (km s^{-1})
245 8862.347322	6.81	1.55	47.88	0.48	6.30	0.01
245 8895.370240	7.25	2.93	47.65	0.48	6.31	0.01
245 8896.359494	6.00	2.43	47.63	0.48	6.33	0.01
245 8897.362492	13.45	3.73	47.60	0.48	6.33	0.01
245 8898.360083	11.97	2.42	47.59	0.48	6.33	0.01
245 9132.716760	9.21	1.95	47.74	0.48	6.31	0.01
245 9148.685964	13.70	2.09	47.65	0.48	6.32	0.01
245 9149.517374	8.89	2.29	47.55	0.48	6.31	0.01
245 9150.532833	9.35	2.03	47.56	0.48	6.31	0.01
245 9151.517034	9.17	2.07	47.51	0.48	6.32	0.01
245 9160.502878	15.68	1.70	47.67	0.48	6.33	0.01
245 9204.441437	−2.40	2.66	47.70	0.48	6.30	0.01
245 9205.480395	5.54	1.83	47.72	0.48	6.31	0.01
245 9206.451903	9.62	1.40	47.77	0.48	6.31	0.01
245 9248.358036	4.97	1.71	47.64	0.48	6.33	0.01
245 9249.359368	4.16	3.00	47.51	0.48	6.34	0.01
245 9265.334407	−9.51	4.33	47.18	0.47	6.33	0.01
245 9268.347483	8.19	1.75	47.74	0.48	6.30	0.01
245 9405.689938	4.49	2.80	47.59	0.48	6.40	0.01
245 9410.640158	9.55	2.32	47.59	0.48	6.40	0.01
245 9432.724961	7.16	1.82	47.68	0.48	6.39	0.01
245 9469.688165	11.85	2.11	47.63	0.48	6.39	0.01
245 9549.505157	7.40	2.02	47.74	0.48	6.37	0.01
245 9572.468757	11.18	2.18	47.74	0.48	6.37	0.01
245 9593.391779	17.27	2.09	47.63	0.48	6.39	0.01
245 9609.368066	21.35	5.28	47.69	0.48	6.35	0.01
245 9610.358438	13.91	2.13	47.79	0.48	6.36	0.01
245 9765.638588	14.07	1.68	47.76	0.48	6.39	0.01
245 9766.632046	11.94	2.72	47.66	0.48	6.39	0.01
245 9785.657277	8.01	2.22	47.77	0.48	6.39	0.01
245 9810.618441	13.44	1.99	47.70	0.48	6.39	0.01
245 9811.612679	14.45	2.43	47.67	0.48	6.39	0.01
245 9812.650632	19.56	2.37	47.64	0.48	6.40	0.01
245 9813.633064	8.83	7.05	47.46	0.47	6.38	0.01
245 9814.644726	11.34	3.19	47.58	0.48	6.40	0.01
245 9882.688144	11.44	2.28	47.77	0.48	6.39	0.01
245 9883.631846	11.95	1.88	47.79	0.48	6.38	0.01
245 9888.505341	9.26	1.52	47.67	0.48	6.39	0.01
245 9888.605016	11.11	1.95	47.63	0.48	6.39	0.01
245 9890.567454	12.63	1.99	47.42	0.47	6.41	0.01
245 9911.499567	16.89	2.65	47.78	0.48	6.36	0.01
245 9912.325684	15.46	1.65	47.85	0.48	6.37	0.01
245 9913.42869	8.73	1.53	47.83	0.48	6.37	0.01
245 9931.372061	28.71	1.87	47.74	0.48	6.39	0.01
245 9934.365966	20.30	1.59	47.84	0.48	6.36	0.01
245 9936.468371	16.31	2.16	47.80	0.48	6.35	0.01
245 9937.396886	15.08	1.81	47.87	0.48	6.35	0.01
245 9950.35306	9.86	2.94	47.48	0.47	6.39	0.01
245 9958.345769	24.79	2.56	47.55	0.48	6.41	0.01
245 9972.412831	10.17	3.51	47.56	0.48	6.40	0.01
245 9989.349576	8.42	3.60	47.48	0.47	6.41	0.01
246 0259.580937	13.23	2.02	47.82	0.48	6.38	0.01

Table A3. Time series of TOI-1472 activity indicators from SERVAL: chromospheric index CRX, differential line width dLW, H α, the sodium lines Na I and Na II, and their related uncertainties.

JD	CRX	σ_{CRX}	DLW	σ_{DLW}	H α	$\sigma_{H\alpha}$	Na I	$\sigma_{Na I}$	Na II	$\sigma_{Na II}$
245 8862.347322	23.63	8.27	−28.15	1.70	0.51	0.01	0.20	0.01	0.25	0.01
245 8895.370240	−1.60	17.34	−11.38	2.71	0.51	0.01	0.22	0.01	0.28	0.01
245 8896.359494	23.98	13.42	−7.68	2.55	0.52	0.01	0.21	0.01	0.27	0.01
245 8897.362492	−16.75	17.86	−13.48	2.66	0.52	0.01	0.23	0.01	0.28	0.01
245 8898.360083	9.59	12.92	−8.03	2.56	0.51	0.01	0.21	0.01	0.27	0.01
245 9132.716760	3.95	9.00	−16.84	2.10	0.52	0.01	0.19	0.01	0.26	0.01
245 9148.685964	16.01	9.54	−7.27	2.07	0.52	0.01	0.20	0.01	0.27	0.01
245 9149.517374	−6.08	12.21	−5.38	2.42	0.52	0.01	0.21	0.01	0.28	0.01
245 9150.532833	−16.76	9.09	−3.36	2.27	0.51	0.01	0.20	0.01	0.26	0.01
245 9151.517034	−12.76	8.13	−4.12	2.49	0.51	0.01	0.20	0.01	0.27	0.01
245 9160.502878	1.04	8.53	−9.93	1.52	0.52	0.01	0.20	0.01	0.26	0.01
245 9204.441437	14.15	12.44	−12.50	2.42	0.51	0.01	0.20	0.01	0.27	0.01
245 9205.480395	3.37	9.78	−14.18	1.95	0.51	0.01	0.20	0.01	0.27	0.01
245 9206.451903	−10.02	6.28	−19.29	1.53	0.51	0.01	0.20	0.01	0.26	0.01
245 9248.358036	0.50	9.79	−7.49	1.68	0.51	0.01	0.19	0.01	0.26	0.01
245 9249.359368	−9.59	13.18	−1.72	2.80	0.51	0.01	0.20	0.01	0.26	0.01
245 9265.334407	44.26	15.77	61.77	4.86	0.52	0.01	0.24	0.01	0.29	0.01
245 9268.347483	7.05	7.65	−17.69	1.75	0.51	0.01	0.20	0.01	0.26	0.01
245 9405.689938	−3.13	13.44	−0.04	2.92	0.51	0.01	0.20	0.01	0.25	0.01
245 9410.640158	7.30	7.95	−3.05	2.28	0.52	0.01	0.20	0.01	0.25	0.01
245 9432.724961	2.88	8.06	−7.96	1.85	0.51	0.01	0.20	0.01	0.25	0.01
245 9469.688165	−1.93	10.47	−5.16	2.07	0.51	0.01	0.19	0.01	0.26	0.01
245 9549.505157	12.38	10.02	−15.38	1.55	0.51	0.01	0.20	0.01	0.27	0.01
245 9572.468757	−7.91	11.05	−16.24	1.79	0.51	0.01	0.20	0.01	0.27	0.01
245 9593.391779	−3.37	8.96	−7.79	1.60	0.52	0.01	0.20	0.01	0.27	0.01
245 9609.368066	−14.65	18.32	−10.66	4.38	0.51	0.01	0.22	0.01	0.29	0.01
245 9610.358438	4.67	10.11	−20.35	1.53	0.51	0.01	0.20	0.01	0.27	0.01
245 9765.638588	1.94	6.40	−12.62	1.65	0.51	0.01	0.19	0.01	0.25	0.01
245 9766.632046	6.07	9.86	−14.33	2.04	0.52	0.01	0.19	0.01	0.25	0.01
245 9785.657277	−6.57	11.67	−20.23	2.13	0.52	0.01	0.20	0.01	0.25	0.01
245 9810.618441	−3.43	9.42	−10.54	1.56	0.51	0.01	0.19	0.01	0.25	0.01
245 9811.612679	−10.00	8.94	−8.06	2.38	0.51	0.01	0.20	0.01	0.26	0.01
245 9812.650632	7.24	11.38	−7.55	1.96	0.52	0.01	0.20	0.01	0.26	0.01
245 9813.633064	−24.04	21.47	−3.28	4.56	0.52	0.01	0.19	0.01	0.25	0.01
245 9814.644727	15.21	13.02	−3.57	2.18	0.52	0.01	0.20	0.01	0.26	0.01
245 9882.688144	−2.98	11.45	−16.69	2.11	0.52	0.01	0.20	0.01	0.27	0.01
245 9883.631846	5.28	9.23	−18.41	1.83	0.52	0.01	0.20	0.01	0.27	0.01
245 9888.505341	−0.91	7.99	−9.26	1.21	0.52	0.01	0.19	0.01	0.27	0.01
245 9888.605016	5.99	8.84	−3.54	1.97	0.52	0.01	0.20	0.01	0.26	0.01
245 9890.567454	−11.51	10.74	9.92	1.97	0.52	0.01	0.20	0.01	0.27	0.01
245 9911.499567	16.49	11.24	−19.50	2.15	0.51	0.01	0.20	0.01	0.26	0.01
245 9912.325684	−8.29	9.56	−23.53	1.24	0.51	0.01	0.19	0.01	0.26	0.01
245 9913.42869	−3.73	7.59	−23.40	1.36	0.52	0.01	0.19	0.01	0.26	0.01
245 9931.372061	−3.25	8.73	−12.81	1.46	0.51	0.01	0.20	0.01	0.26	0.01
245 9934.365966	−3.90	7.93	−21.81	1.21	0.51	0.01	0.19	0.01	0.26	0.01
245 9936.468371	5.25	10.16	−25.49	1.96	0.51	0.01	0.20	0.01	0.26	0.01
245 9937.396886	2.11	8.61	−24.46	1.72	0.51	0.01	0.19	0.01	0.26	0.01
245 9950.35306	−11.10	13.07	1.22	2.56	0.51	0.01	0.20	0.01	0.27	0.01
245 9958.345769	−32.08	10.25	2.52	2.17	0.52	0.01	0.20	0.01	0.27	0.01
245 9972.412831	2.46	15.27	−5.60	2.92	0.52	0.01	0.21	0.01	0.27	0.01
245 9989.349576	−22.20	15.77	4.76	3.11	0.52	0.01	0.21	0.01	0.28	0.01
246 0259.580937	12.21	11.37	−19.00	1.92	0.50	0.01	0.20	0.01	0.27	0.01

Table A4. Time series of TOI-1648 from HARPS-N data: Julian dates, RVs, S-index, log R'_{HK}, and their related uncertainties.

JD	RV (m s^{-1})	σ_{RV} (m s^{-1})	S-index	$\sigma_{S\text{-index}}$	log R'_{HK}	$\sigma_{\log R'_{HK}}$
245 9132.740420	−32044.46	0.80	0.255	0.004	−4.94	0.01
245 9148.710324	−32051.06	1.14	0.270	0.003	−4.92	0.00
245 9149.605233	−32053.28	0.92	0.257	0.004	−4.94	0.01
245 9150.615213	−32049.72	0.69	0.258	0.005	−4.94	0.01
245 9151.599589	−32048.24	0.80	0.306	0.006	−4.86	0.01
245 9160.585645	−32047.62	0.95	0.302	0.004	−4.86	0.01
245 9204.475924	−32044.22	1.05	0.314	0.006	−4.85	0.01
245 9205.513825	−32043.77	0.91	0.286	0.003	−4.89	0.00
245 9206.513098	−32042.40	1.09	0.271	0.006	−4.92	0.01
245 9248.392205	−32045.97	0.64	0.272	0.003	−4.91	0.00
245 9265.360498	−32043.46	1.17	0.255	0.007	−4.95	0.01
245 9268.373439	−32049.35	0.66	0.241	0.004	−4.97	0.01
245 9451.739271	−32045.06	1.19	0.255	0.006	−4.94	0.01
245 9452.748155	−32048.88	0.87	0.276	0.015	−4.91	0.03
245 9469.708267	−32048.50	1.08	0.262	0.006	−4.93	0.01
245 9470.678768	−32050.08	2.12	0.276	0.006	−4.91	0.01
245 9549.526062	−32044.14	0.99	0.276	0.005	−4.91	0.01
245 9571.512639	−32045.60	0.94	0.260	0.017	−4.94	0.03
245 9573.533827	−32048.01	0.92	0.258	0.006	−4.94	0.01
245 9574.527225	−32049.44	1.55	0.310	0.004	−4.85	0.01
245 9610.427829	−32046.98	0.98	0.276	0.006	−4.91	0.01
245 9765.667457	−32049.90	0.83	0.255	0.005	−4.94	0.01
245 9766.664999	−32050.12	0.99	0.233	0.006	−4.99	0.01
245 9785.695006	−32048.95	2.60	0.202	0.023	−5.06	0.06
245 9810.670124	−32048.42	1.09	0.248	0.007	−4.96	0.01
245 9811.689098	−32046.79	1.13	0.252	0.007	−4.95	0.01
245 9812.695747	−32046.59	1.30	0.262	0.009	−4.93	0.02
245 9813.712035	−32047.06	2.24	0.260	0.019	−4.94	0.03
245 9814.690624	−32048.86	0.96	0.257	0.005	−4.94	0.01
245 9851.716994	−32052.63	1.29	0.252	0.008	−4.95	0.02
245 9882.709453	−32055.26	0.99	0.230	0.006	−4.99	0.01
245 9883.675674	−32053.75	0.84	0.223	0.004	−5.01	0.01
245 9888.527053	−32048.81	0.67	0.238	0.003	−4.98	0.01
245 9892.415132	−32045.97	1.13	0.239	0.007	−4.98	0.01
245 9894.570115	−32047.86	0.83	0.245	0.004	−4.96	0.01
245 9913.479118	−32048.92	0.74	0.227	0.003	−5.00	0.01
245 9932.564677	−32045.99	1.23	0.246	0.008	−4.96	0.02
245 9934.456529	−32046.83	0.72	0.244	0.003	−4.97	0.01
245 9937.483906	−32045.17	0.76	0.242	0.004	−4.97	0.01
245 9943.448201	−32047.42	5.89	0.265	0.067	−4.93	0.12
245 9950.538722	−32050.46	1.67	0.236	0.013	−4.98	0.03
245 9959.487041	−32042.58	1.36	0.250	0.009	−4.95	0.02
245 9962.433216	−32052.73	1.13	0.225	0.007	−5.01	0.02
245 9973.475613	−32046.86	1.48	0.243	0.011	−4.97	0.02
245 9989.386713	−32047.47	1.11	0.235	0.007	−4.98	0.01
245 9990.378141	−32050.18	1.50	0.230	0.011	−4.99	0.02
245 9995.428123	−32041.57	0.78	0.244	0.004	−4.97	0.01
246 0002.351716	−32045.54	0.67	0.247	0.003	−4.96	0.01
246 0005.367204	−32047.99	0.61	0.244	0.003	−4.97	0.01
246 0007.354761	−32049.50	0.94	0.243	0.006	−4.97	0.01
246 0009.365213	−32050.37	0.64	0.231	0.003	−4.99	0.01
246 0014.342538	−32052.81	1.00	0.234	0.006	−4.99	0.01
246 0259.620739	−32044.95	0.90	0.237	0.005	−4.98	0.01

Table A5. Time series of additional TOI-1648 activity indicators from HARPS-N DRS: bisector, CCF contrast, CCF FWHM, and their related uncertainties.

JD	BIS (m s^{-1})	σ_{BIS} (m s^{-1})	CONT (km s^{-1})	σ_{CONT} (km s^{-1})	FWHM (km s^{-1})	σ_{FWHM} (km s^{-1})
245 9132.740420	14.85	1.13	50.90	0.51	6.28	0.01
245 9148.710324	14.73	1.61	51.05	0.51	6.26	0.01
245 9149.605233	13.76	1.30	51.06	0.51	6.26	0.01
245 9150.615213	12.08	0.98	51.08	0.51	6.25	0.01
245 9151.599589	13.66	1.13	51.07	0.51	6.25	0.01
245 9160.585645	7.81	1.35	51.04	0.51	6.25	0.01
245 9204.475924	9.43	1.49	50.92	0.51	6.28	0.01
245 9205.513825	11.39	1.29	50.95	0.51	6.28	0.01
245 9206.513098	13.38	1.54	50.90	0.51	6.28	0.01
245 9248.392205	10.29	0.91	51.04	0.51	6.27	0.01
245 9265.360498	5.94	1.65	50.99	0.51	6.26	0.01
245 9268.373439	11.62	0.93	51.01	0.51	6.26	0.01
245 9451.739271	11.90	1.68	51.03	0.51	6.32	0.01
245 9452.748155	11.14	1.23	50.91	0.51	6.32	0.01
245 9469.708267	6.37	1.53	51.19	0.51	6.32	0.01
245 9470.678768	4.01	2.99	51.06	0.51	6.31	0.01
245 9549.526062	7.63	1.40	51.30	0.51	6.30	0.01
245 9571.512639	10.28	1.33	51.28	0.51	6.30	0.01
245 9573.533827	17.46	1.30	51.31	0.51	6.30	0.01
245 9574.527225	11.67	2.19	51.30	0.51	6.28	0.01
245 9610.427829	13.86	1.38	51.29	0.51	6.30	0.01
245 9765.667457	10.19	1.18	51.38	0.51	6.29	0.01
245 9766.664999	11.75	1.40	51.36	0.51	6.30	0.01
245 9785.695006	13.14	3.68	51.33	0.51	6.29	0.01
245 9810.670124	11.35	1.55	51.33	0.51	6.30	0.01
245 9811.689098	15.39	1.60	51.35	0.51	6.30	0.01
245 9812.695747	7.32	1.84	51.35	0.51	6.30	0.01
245 9813.712035	7.40	3.17	51.24	0.51	6.30	0.01
245 9814.690624	11.97	1.35	51.37	0.51	6.30	0.01
245 9851.716994	4.44	1.82	51.36	0.51	6.30	0.01
245 9882.709453	6.50	1.39	51.49	0.51	6.28	0.01
245 9883.675674	−0.85	1.19	51.48	0.51	6.28	0.01
245 9888.527053	4.50	0.95	51.38	0.51	6.29	0.01
245 9892.415132	4.85	1.60	51.16	0.51	6.30	0.01
245 9894.570115	11.35	1.17	51.26	0.51	6.30	0.01
245 9913.479118	9.09	1.04	51.48	0.51	6.28	0.01
245 9932.564677	5.06	1.74	51.37	0.51	6.29	0.01
245 9934.456529	4.69	1.02	51.36	0.51	6.29	0.01
245 9937.483906	13.48	1.07	51.38	0.51	6.29	0.01
245 9943.448201	14.98	8.33	51.08	0.51	6.28	0.01
245 9950.538722	8.60	2.37	51.07	0.51	6.29	0.01
245 9959.487041	10.53	1.92	51.39	0.51	6.28	0.01
245 9962.433216	8.41	1.60	51.43	0.51	6.29	0.01
245 9973.475613	1.52	2.09	51.39	0.51	6.28	0.01
245 9989.386713	5.40	1.56	51.47	0.51	6.28	0.01
245 9990.378141	1.74	2.12	51.40	0.51	6.28	0.01
245 9995.428123	3.66	1.10	51.38	0.51	6.29	0.01
246 0002.351716	7.09	0.95	51.34	0.51	6.30	0.01
246 0005.367204	10.33	0.87	51.36	0.51	6.29	0.01
246 0007.354761	11.21	1.33	51.38	0.51	6.29	0.01
246 0009.365213	11.50	0.90	51.41	0.51	6.28	0.01
246 0014.342538	4.89	1.41	51.38	0.51	6.28	0.01
246 0259.620739	6.46	1.28	51.51	0.52	6.28	0.01

Table A6. Time series of TOI-1648 activity indicators from SERVAL: chromospheric index CRX, differential line width dLW, H α, the sodium lines Na I and Na II, and their related uncertainties.

JD	CRX	$\sigma_{\rm CRX}$	DLW	$\sigma_{\rm DLW}$	H α	$\sigma_{\rm H\,\alpha}$	Na I	$\sigma_{\rm Na\,I}$	Na II	$\sigma_{\rm Na\,II}$
245 9132.740420	−5.56	6.22	21.90	1.95	0.55	0.01	0.18	0.01	0.22	0.01
245 9148.710324	1.90	8.76	5.41	1.65	0.55	0.01	0.18	0.01	0.23	0.01
245 9149.605233	−12.80	6.20	5.27	1.53	0.55	0.01	0.17	0.01	0.22	0.01
245 9150.615213	−3.54	6.13	3.68	1.27	0.55	0.01	0.18	0.01	0.22	0.01
245 9151.599589	1.85	6.42	3.71	1.30	0.55	0.01	0.18	0.01	0.22	0.01
245 9160.585645	−4.68	8.81	5.62	1.56	0.55	0.01	0.17	0.01	0.22	0.01
245 9204.475924	18.16	8.66	16.15	1.67	0.55	0.01	0.17	0.01	0.22	0.01
245 9205.513825	9.42	7.20	16.43	1.60	0.55	0.01	0.17	0.01	0.22	0.01
245 9206.513098	−14.48	7.43	18.86	1.86	0.55	0.01	0.17	0.01	0.23	0.01
245 9248.392205	−6.06	5.20	5.61	1.46	0.55	0.01	0.17	0.01	0.22	0.01
245 9265.360498	4.44	8.19	8.99	1.97	0.55	0.01	0.18	0.01	0.23	0.01
245 9268.373439	−14.69	5.76	7.52	1.37	0.55	0.01	0.18	0.01	0.23	0.01
245 9451.739271	0.83	8.89	7.91	2.51	0.55	0.01	0.17	0.01	0.22	0.01
245 9452.748155	−0.98	6.94	24.15	1.91	0.55	0.01	0.17	0.01	0.22	0.01
245 9469.708267	0.51	7.88	−0.06	1.57	0.55	0.01	0.17	0.01	0.22	0.01
245 9470.678768	−6.67	13.67	6.34	2.91	0.55	0.01	0.18	0.01	0.22	0.01
245 9549.526062	4.85	7.41	−12.22	1.39	0.55	0.01	0.17	0.01	0.23	0.01
245 9571.512639	3.24	7.47	−11.03	1.28	0.54	0.01	0.17	0.01	0.23	0.01
245 9573.533827	13.63	6.96	−13.96	1.08	0.55	0.01	0.17	0.01	0.23	0.01
245 9574.527225	−18.74	10.97	−16.49	1.62	0.55	0.01	0.17	0.01	0.23	0.01
245 9610.427829	−5.00	7.90	−10.43	1.21	0.54	0.01	0.17	0.01	0.23	0.01
245 9765.667457	2.74	7.80	−18.40	0.88	0.55	0.01	0.17	0.01	0.22	0.01
245 9766.664999	1.31	7.57	−18.53	1.15	0.54	0.01	0.17	0.01	0.22	0.01
245 9785.695006	30.28	14.15	−20.39	2.65	0.55	0.01	0.18	0.01	0.23	0.01
245 9810.670124	16.24	8.04	−17.62	1.46	0.54	0.01	0.17	0.01	0.22	0.01
245 9811.689098	−8.98	7.00	−16.47	1.56	0.55	0.01	0.17	0.01	0.22	0.01
245 9812.695747	−6.33	8.53	−18.76	1.58	0.55	0.01	0.18	0.01	0.22	0.01
245 9813.712035	−6.98	13.68	−7.89	2.59	0.54	0.01	0.18	0.01	0.23	0.01
245 9814.690624	4.44	6.70	−20.07	1.40	0.55	0.01	0.17	0.01	0.22	0.01
245 9851.716994	5.35	8.31	−20.11	1.87	0.55	0.01	0.18	0.01	0.22	0.01
245 9882.709453	11.01	6.54	−31.02	1.45	0.55	0.01	0.18	0.01	0.22	0.01
245 9883.675674	4.92	5.90	−29.92	1.23	0.55	0.01	0.17	0.01	0.22	0.01
245 9888.527053	6.02	5.52	−18.57	0.90	0.55	0.01	0.17	0.01	0.22	0.01
245 9892.415132	5.45	8.75	−3.48	1.43	0.55	0.01	0.17	0.01	0.23	0.01
245 9894.570115	−8.39	6.66	−7.05	1.09	0.55	0.01	0.17	0.01	0.23	0.01
245 9913.479118	−0.96	6.08	−28.63	1.06	0.55	0.01	0.17	0.01	0.22	0.01
245 9932.564677	26.11	9.66	−19.48	1.57	0.55	0.01	0.17	0.01	0.23	0.01
245 9934.456529	2.03	6.47	−17.58	1.06	0.56	0.01	0.17	0.01	0.23	0.01
245 9937.483906	5.07	5.60	−18.93	1.03	0.55	0.01	0.17	0.01	0.23	0.01
245 9943.448201	13.22	25.91	−15.07	6.58	0.56	0.01	0.17	0.01	0.24	0.01
245 9950.538722	−5.24	9.58	1.25	2.74	0.55	0.01	0.17	0.01	0.23	0.01
245 9959.487041	−13.65	8.56	−24.37	1.88	0.55	0.01	0.17	0.01	0.23	0.01
245 9962.433216	−13.88	7.81	−25.37	1.32	0.56	0.01	0.17	0.01	0.23	0.01
245 9973.475613	7.82	8.86	−22.48	2.22	0.55	0.01	0.18	0.01	0.23	0.01
245 9989.386713	−13.72	7.10	−29.78	1.32	0.55	0.01	0.17	0.01	0.23	0.01
245 9990.378141	0.24	9.05	−25.93	2.19	0.55	0.01	0.18	0.01	0.23	0.01
245 9995.428123	7.13	6.66	−21.60	1.17	0.55	0.01	0.18	0.01	0.23	0.01
246 0002.351716	4.15	6.00	−15.06	0.72	0.55	0.01	0.17	0.01	0.23	0.01
246 0005.367204	−5.41	5.54	−17.27	0.82	0.55	0.01	0.17	0.01	0.23	0.01
246 0007.354761	−8.37	7.65	−19.78	1.38	0.55	0.01	0.17	0.01	0.23	0.01
246 0009.365213	2.92	6.54	−23.82	0.87	0.56	0.01	0.17	0.01	0.23	0.01
246 0014.342538	15.00	6.85	−6.57	2.83	0.55	0.01	0.18	0.01	0.23	0.01
246 0259.620739	5.95	8.53	−26.77	1.57	0.52	0.01	0.17	0.01	0.22	0.01

[1]INAF – Osservatorio Astrofisico di Torino, Via Osservatorio 20, I-10025 Pino Torinese, Italy
[2]Instituto de Astrofísica de Canarias (IAC), E-38205 La Laguna, Tenerife, Spain
[3]Institute of Astronomy, Faculty of Physics, Astronomy and Informatics, Nicolaus Copernicus University, Grudziądzka 5, PL-87-100 Toruń, Poland
[4]Departamento de Astrofísica, Universidad de La Laguna (ULL), E-38206 La Laguna, Tenerife, Spain
[5]Astronomical Observatory, University of Geneva, Chemin Pegasi 51b, CH-1290 Versoix, Switzerland
[6]Centro de Astrofísica y Tecnologías Afines (CATA), Casilla 36-D, 7591245 Santiago, Chile
[7]Núcleo de Astronomía, Facultad de Ingeniería y Ciencias, Universidad Diego Portales, Av. Ejército 441, 8370191, Santiago, Chile
[8]Departamento de Astronomía, Universidad de Chile, Casilla 36-D, 7591245 Santiago, Chile
[9]Instituto de Astronomía, Universidad Católica del Norte, Angamos 0610, 1270709 Antofagasta, Chile
[10]Department of Physics & Astronomy, Vanderbilt University, Nashville, TN 37235, USA
[11]Dipartimento di Fisica, Universitá degli Studi di Torino, Via Pietro Giuria 1, I-10125 Torino, Italy
[12]INAF – Osservatorio Astrofisico di Catania, Via S. Sofia 78, I-95123 Catania, Italy
[13]NASA Exoplanet Science Institute, IPAC, California Institute of Technology, Pasadena, CA 91125, USA
[14]Center for Astrophysics | Harvard & Smithsonian, 60 Garden Street, Cambridge, MA 02138, USA
[15]Astrophysics Group, Keele University, Staffs ST5 5BG, UK
[16]Thüringer Landessternwarte, Sternwarte 5, D-07778 Tautenburg, Germany
[17]NASA Ames Research Center, Moffett Field, CA 94035, USA
[18]Stellar Astrophysics Centre, Department of Physics and Astronomy, Aarhus University, Ny Munkegade 120, DK-8000 Aarhus C, Denmark
[19]Chalmers University of Technology, Department of Space, Earth and Environment, Onsala Space Observatory, SE-43992 Onsala, Sweden
[20]Centro de Astrobiología (CAB, CSIC-INTA), Depto de Astrofísica, ESAC Campus, E-28692 Villanueva de la Cañada, Madrid, Spain
[21]Astrobiology Center, 2-21-1 Osawa, Mitaka, Tokyo 181-8588, Japan
[22]National Astronomical Observatory of Japan, 2-21-1 Osawa, Mitaka, Tokyo 181-8588, Japan
[23]Department of Astronomy, The Graduate University for Advanced Studies (SOKENDAI), 2-21-1 Osawa, Mitaka, Tokyo 181-8588, Japan
[24]The University of Texas at Austin, 2515 Speedway, Stop C1402, Austin, TX 78712-1206, USA
[25]Astronomy Department and Van Vleck Observatory, Wesleyan University, Middletown, CT 06459, USA
[26]Sternberg Astronomical Institute, Lomonosov Moscow State University, Universitetskii Prospekt 13, 119992 Moscow, Russia
[27]Physics Department, Austin College, Sherman, TX 75090, USA
[28]Department of Physics and Astronomy, University of North Carolina at Chapel Hill, Chapel Hill, NC 27599, USA
[29]Observatori Astronòmic Albanyà, Camí de Bassegoda s/n, E-17733 Albanyà, Girona, Spain
[30]Komaba Institute for Science, The University of Tokyo, 3-8-1 Komaba, Meguro, Tokyo 153-8902, Japan
[31]Department of Physical Sciences, Ritsumeikan University, Kusatsu, Shiga 525-8577, Japan
[32]Sabadell Astronomical Society, E-08206 Sabadell, Barcelona, Spain
[33]Europlanet Society, Department of Planetary Atmospheres of the Royal Belgian Institute for Space Aeronomy, B-1180 Brussels, Belgium
[34]Instituto de Astrofísica de Andalucía (IAA-CSIC), Glorieta de la Astronomía s/n, E-18008 Granada, Spain
[35]Villa ’39 Observatory, Landers, CA 92285, USA
[36]Waffelow Creek Observatory, 10780 FM 1878, Nacogdoches, TX 75961, USA
[37]INAF – Osservatorio Astronomico di Palermo, Piazza del Parlamento 1, I-90134 Palermo, Italy
[38]Department of Physics and Kavli Institute for Astrophysics and Space Research, Massachusetts Institute of Technology, Cambridge, MA 02139, USA
[39]Bozeman, MT 59718, USA

This paper has been typeset from a TEX/LATEX file prepared by the author.